Tampere University

Raymond Quinn

DESIGN AND MODELLING OF FILTER INDUCTORS FOR DC/AC CONVERTERS

Master of Science Thesis
Faculty of Information Technology and Communication Sciences
Examiners: Associate Professor Paavo Rasilo
Joonas Vesa DSc
November 2022

ABSTRACT

Raymond Quinn: Design and Modelling of Filter Inductors for DC/AC Converters
Master of Science Thesis
Tampere University
Master's Programme in Electrical Engineering
November 2022

DC/AC converters are power electronic devices which convert direct current (DC) electricity into alternating current (AC) electricity. They are known as inverters and are commonly used to connect renewable energy resources to the electricity grid, or to drive motors in electric transportation applications amongst many other uses. In the race to combat global climate change and reduce carbon emissions, the prevalence of renewable energy resources and electric transportation is set to increase, and with it, the need for energy efficient, low cost, and compact power electronic converters as an enabling technology.

Inverter output needs to be conditioned using passive components as filters since it contains high levels of unwanted harmonic content which leads to undesirable effects in power systems and electrical machines. Strict industry standards dictate the level of filtering required. Passive components remain a stumbling block in improving the size, cost, and efficiency of inverter systems. It is for this reason that the development of fast and accurate design and modelling tools for passive components is needed in order to easily study and optimise their performance.

In this thesis, a way of rapidly designing, modelling, and constructing filter inductors for DC/AC inverters is investigated. A design tool is developed to provide multiple design possibilities by varying geometric parameters. The designs are then analysed using a MATLAB Simulink inductor model which provides accurate information about the losses in the designed inductors. Of the hundreds of inductors designed, a few are selected to be constructed in an effort to validate the design tool and simulation model. The construction process highlighted challenges in prototyping inductors with non-standard geometries. Recommendations are given on how to improve the design tool, simulation model and construction process going forward.

Keywords: area-product method, core losses, filter inductors, harmonics, inverters

The originality of this thesis has been checked using the Turnitin Originality Check service.

PREFACE

I would like to thank Associate Professor Paavo Rasilo for his advice and assistance during this master's thesis project and also for the opportunity to work on many interesting projects as part of the Electromechanics research group at Tampere University. Thanks also to Joonas Vesa, Umair Ahmed, Jay Panchal, and Alex Aaltonen for their assistance in practical matters related to the thesis. Finally, I would like to thank my family and friends for their support during the course of my studies.

Tampere, 28 November 2022

Raymond Quinn

CONTENTS

1. INTRODUCTION 1
2. BACKGROUND STUDIES 4
2.1 Inverters 4
2.1.1 Half-bridge inverter 5
2.1.2 Full-bridge inverter 7
2.1.3 Harmonics 8
2.1.4 Pulse-width modulation control 10
2.1.5 Bipolar modulation 11
2.1.6 Unipolar modulation 12
2.2 Filter inductors 14
2.2.1 Electromagnetic principles 15
2.2.2 Materials 18
2.2.3 Losses in inductors 19
2.2.4 Winding losses 20
2.2.5 Core losses 22
3. DESIGN AND SIMULATION METHODS 26
3.1 Area-product design method 26
3.2 Filter inductor design procedure 31
3.3 Simulink inductor model 33
4. DESIGN AND SIMULATION RESULTS 37
4.1 Filter inductor design results 37
4.2 Filter inductor simulation results 40
5. EXPERIMENTAL VALIDATION 47
5.1 Selected cores 47
5.2 Construction process 48
5.3 Measurement results 50
6. CONCLUSIONS 55
REFERENCES 56
APPENDIX A 61
APPENDIX B 63

LIST OF SYMBOLS AND ABBREVIATIONS

α	Steinmetz coefficient for frequency
β	Steinmetz coefficient for flux density
δ	skin depth
λ	magnetic flux linkage
μ	absolute permeability
μ_{e}	effective permeability of gapped core
μ_{d}	differential permeability
μ_{r}	relative permeability
μ_0	permeability of free space
ρ	resistivity of conductor
σ	conductivity of core
Φ	magnetic flux
A_0	Dowell's equation factor
A_{c}	cross-sectional area of a surface
A_{Cu}	cross-sectional area of conductor
A_{p}	area-product
b_0	average flux density
b	magnetic flux density
$\boldsymbol{B}$	magnetic flux density vector
B_{m}	maximum flux density
B_{r}	remanent flux density
B_{sat}	saturation flux density
c_{ex}	excess loss coefficient
C	excess loss coefficient
d	lamination thickness
d_{Cu}	conductor diameter
d_{i}	inner diameter of toroid
d_{o}	outer diameter of toroid
f	frequency
f_{control}	control signal frequency
$f_{\mathrm{fundamental}}$	fundamental frequency
f_n	frequency of nth harmonic
f_{sw}	switching frequency
f_{tri}	carrier signal frequency
$\mathcal{F}$	magnetomotive force
F_{f}	fringing factor
F_{R}	AC-to-DC winding resistance ratio
h	core height
h_{hy}	local magnetic field strength
h_{s}	surface magnetic field strength
$\boldsymbol{H}$	magnetic field strength vector
H_{c}	coercive field strength
i	current
i_{AC}	AC winding current
i_{DC}	DC winding current
i_{L}	inductor current
$i_{\mathrm{pp,max}}$	maximum peak-to-peak ripple current

I	RMS current
I_m	current amplitude
J_m	current density amplitude
k_1	ratio of bare and insulated conductor diameter
k_2	fill factor
k_3	effective winding window
k_4	insulation factor
k_d	ratio between core inner and outer diameter
k_h	Steinmetz coefficient for hysteresis losses
k_e	Steinmetz coefficient for eddy current losses
k_u	window utilisation factor
l_c	mean magnetic path length
l_Cu	conductor length
l_g	air gap length
L	inductance
L_ref	required inductance value
L_σ	leakage inductance
m_a	amplitude modulation ratio
n	harmonic order
N	number of winding turns
N_l	number of winding layers
p_cl	power density of eddy current losses
p_ex	power density of excess losses
p_h	power density of hysteresis losses
p_hy	power density for rate-of-change of magnetic field energy
P_AC	AC winding losses
P_cl	eddy current losses
P_core	core losses
P_DC	DC winding losses
P_ex	excess losses
P_hy	hysteresis losses
$P_\mathrm{lamination}$	resistive losses in lamination
P_r	resistive losses in solid core
P_total	total losses
P_winding	winding losses
r	radial distance from centre of conductor
R	winding resistance
R_AC	AC winding resistance
R_DC	DC winding resistance
R_L	load resistance
$\mathcal{R}_\mathrm{core}$	reluctance of core
$\mathcal{R}_\mathrm{gap}$	reluctance of air gap
$\mathcal{R}_\mathrm{gap,f}$	reluctance of air gap with fringing effect
$\mathcal{R}_\mathrm{total}$	total reluctance
$\boldsymbol{S}$	open surface
S_k , k=1,2…	inverter switch
T	period of waveform
T_s	switching period
v_c	voltage induced in core
v_control	PWM reference signal
v_L	inductor voltage
v_n	RMS output voltage of nth harmonic
v_o	inverter output voltage

v_{tri}	PWM carrier signal
$V_{1_{\mathrm{RMS}}}$	fundamental component of output voltage
V_{DC}	inverter input voltage
W_{m}	magnetic energy
W_{a}	winding window area
AC	alternating current
DC	direct current
EDM	electric discharge machining
IGBT	insulated-gate bipolar transistor
MMF	magnetomotive force
PWM	pulse-width modulation
RMS	root mean square
SPWM	sinusoidal pulse-width modulation
THD	total harmonic distortion
UPS	uninterruptible power supply

1. INTRODUCTION

DC/AC converters are power electronic devices used to convert DC electricity to AC electricity using semiconductor switches. They are commonly known as inverters. Inverters are used in a wide variety of applications such as in electric vehicles, to convert the DC power from the on-board battery to AC power to drive the electric motor, or in renewable energy applications, such as converting the DC power produced by a solar panel into AC power to connect to the grid. They are also used in AC/DC/AC systems used to convert the power produced by wind turbines to grid frequency and in uninterruptible power supplies (UPS), to convert DC power from a battery into AC power in the event of a loss of supply from the grid. It is estimated that around 70% of electricity passes through power electronic converters before reaching the end user [1].

In the face of global climate change, and as governments attempt to meet their commitments to reduce carbon emissions, renewable energy solutions and electric transportation will become even more prevalent in the near future. This will lead to the increase in the need for efficient power electronic systems as an enabling technology, and it is expected that upwards of 80% of electricity will be processed by power electronics in a sustainable society [2].

With the increase in the prevalence of power electronic converters comes the need to increase their efficiency and power density whilst reducing their production costs, size and weight. To this end, much work has been carried out in advancing semiconductor technology and control strategies for power electronic converters as well as devising new topologies – the specific arrangement of components in the electrical circuits [3] – but it is the passive components, especially magnetics, of power electronic systems which are the main limiting factor in the improvement of power density and efficiency [4]. The three fundamental passive components are resistors, capacitors, and inductors, of which inductors are electromagnetic components [5]. Passive components contribute considerably to the size and cost of power electronic systems [6], and in some instances can make up over 50% of the mass and volume of a converter [7], with passive components weighing hundreds of kilograms in multi-megawatt systems [8].

The output power of an inverter is required to be filtered using passive components in order to connect to the electricity grid. This is because the output voltage and current of the inverter are non-sinusoidal due to the switching patterns of the semiconductor switches in the inverter. Connecting the inverter to the grid without filtering can lead to power quality issues. Unconditioned inverter output can introduce harmonic currents into the power system leading to the malfunctioning of power system equipment. There are strict industry standards related to current harmonic-producing devices and their connection to the grid, specifically IEEE 519-2014 and IEEE 1547-2018. Some common filters are the L-filter, consisting of one inductor, the LC-filter, consisting of an inductor and capacitor, and the LCL-filter, consisting of two inductors and a capacitor.

One important consideration when designing output filters is the output current ripple – the difference between instantaneous and fundamental current [9]. Current ripple can lead to electromagnetic and radio frequency interference, overheating of motor drives, and other issues [10], [11]. One way to reduce current ripple is to increase the inductance of the filter inductor or to increase the switching frequency of the inverter switches [12]. Increasing the inductance of the filter inductor will increase its physical size and increasing the switching frequency will lead to reduced efficiency due to the increase in switching losses, so there is a trade-off to be made when designing inductors for these purposes. The inductor has to be sized appropriately to minimise temperature rise whilst maintaining good efficiency [13].

In general, inductors are made from a conductive material such as copper which has been wound into a coil. Often this coil is wound around a ferromagnetic core. For the same value of inductance, the use of a core can greatly reduce the physical volume of the inductor and reduce winding losses amongst other advantages [14]. The core makes up the bulk of the weight of a filter inductor, and when building inductors, often has to be selected from pre-made, standard, off-the-shelf solutions due to the expense of manufacturing bespoke shapes and sizes. This can restrict innovation in novel core design and the closest available ready-made option which meets requirements must be chosen, often being larger than the calculated requirement to ensure the core does not overheat or saturate [7]. Extensive optimisation efforts are required to achieve compact designs [15].

Since the desire is to reduce the volume, weight and cost of inductors, new methods and software tools are needed to optimise the design of magnetic components [16] along with cost-effective rapid prototyping techniques for testing purposes. The goal of

this thesis is to find a method of quickly designing and producing toroidal filter inductors for DC/AC inverters. To this end, a procedure for designing toroidal filter inductors using the area-product method varying geometric parameters is introduced. The performance of the designed inductors is then analysed using a MATLAB Simulink inductor model. Finally, selected cores are chosen to be manufactured using different techniques and measurements carried out to test the validity of the design method and Simulink model.

The thesis is outlined as follows: Chapter 2 provides a brief overview of inverters, their control and related power quality issues as well as electromagnetic principles relevant to filter inductors. Chapter 3 describes the design and modelling methods for filter inductors used in this thesis. Chapter 4 shows the design and simulation model results. In Chapter 5, experimental validation of selected filter inductors prototypes is detailed and in Chapter 6 conclusions are drawn about the results and suggestions for future work are given.

2. BACKGROUND STUDIES

In this chapter the basic principles of DC/AC inverters are described. Common inverter topologies, power quality issues and control methods are discussed. Also discussed in this chapter are electromagnetic principles relevant to filter inductor design.

2.1 Inverters

Inverters are devices for converting DC power into AC power. The applications are numerous and varied. The inverter circuit consists of semiconductor switches which turn on and off in a specific sequence. The switches are usually made from insulated-gate bipolar transistors (IGBT), metal–oxide–semiconductor field-effect transistors, silicon carbide or gallium nitride devices depending on the application. In Figure 1 different switch types are shown with reference to the basic inverter circuit. During the on-state, the switch conducts electricity and current flows through it. When the switch is in the off-state, it does not conduct. As can be seen in Figure 1, antiparallel-diodes accompany each switch to ensure a return path for load current when the switch is open. In this thesis, the inverter with fixed output voltage and frequency is considered. Such inverters are most commonly used as power supplies in renewable energy applications, UPS or energy storage applications. They are known as constant voltage constant frequency inverters as opposed to variable voltage variable frequency inverters used in AC motor drive applications [17].

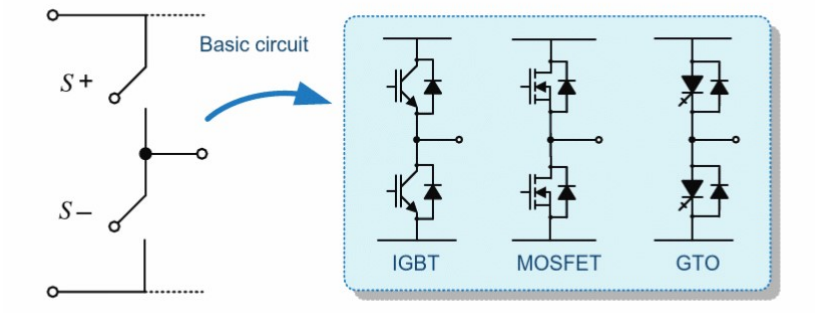

Figure 1: *Different switch types with reference to basic inverter circuit* [17]

2.1.1 Half-bridge inverter

There are a number of different inverter topologies, with the two main single-phase topologies being half-bridge and full-bridge. Single-phase inverters can be combined to create three-phase topologies. Figure 2 shows the basic half-bridge inverter circuit with a DC voltage source and two switches S_1 and S_2. The arrangement of two switches in this manner is known as a leg.

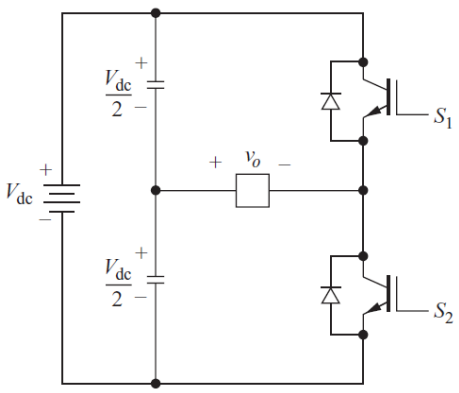

Figure 2: *Half-bridge inverter circuit* [18]

In the half-bridge arrangement, the output voltage (v_o) can be equal to either $\frac{V_{DC}}{2}$ or $-\frac{V_{DC}}{2}$. When switch S_1 is closed and S_2 is open, the output voltage will be

$$V_o = \frac{V_{DC}}{2}. \tag{1}$$

When switch S_2 is closed and switch S_1 is closed, the output voltage will be

$$V_o = -\frac{V_{DC}}{2}. \tag{2}$$

Both switches being open will result in an open circuit and no current will flow, and both switches being closed will result in a short circuit condition called a shoot-through fault which should be avoided as it can damage or destroy the switches [18]. The time taken for the switches to open and close needs to be taken into account to avoid any overlap of switch on-times in a single leg. The root mean square (RMS) value of the fundamental component of the output voltage ($V_{1_{RMS}}$) is calculated as:

$$V_{1_{RMS}} = \frac{1}{\sqrt{2}}\frac{2V_{DC}}{\pi} = 0.45V_{DC}, \tag{3}$$

meaning only 45% of the input DC voltage is achieved at the output. Figure 3 shows the output voltage of the half-bridge inverter when square wave modulation is used. The square wave modulation technique consists of alternating each switch between on and off each half period $\left(\frac{T}{2}\right)$ for a given frequency. This results in an AC signal at the output of the inverter. This simple method has the advantage of low switching losses, but due to the non-sinusoidal nature of the output voltage, high amounts of harmonic distortion are present, leading to the need for large filter inductors – adding size and weight and contributing to higher losses [19]. For a purely resistive load, the current waveform will match the shape of the voltage waveform. For an inductive load the current will become more sinusoidal as shown in Figure 4 due to the filtering effect of inductance [18] .

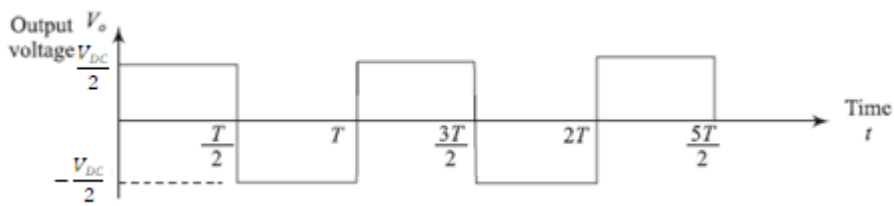

Figure 3: *Output voltage of square wave half-bridge inverter* [20]

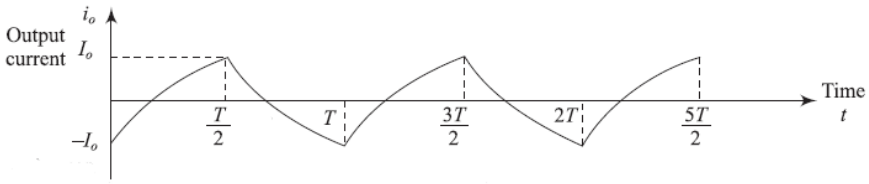

Figure 4: *Output current of square wave half-bridge inverter with inductive load* [20]

2.1.2 Full-bridge inverter

The basic circuit of the full-bridge inverter - often called the H-bridge inverter due to the layout of the circuit - is shown in Figure 5. In contrast with the half-bridge inverter, it features two legs and four switches. The full-bridge inverter is capable of producing V_{DC} and $-V_{\mathrm{DC}}$ at its output as opposed to $\frac{V_{\mathrm{DC}}}{2}$ and $-\frac{V_{\mathrm{DC}}}{2}$ produced by the half-bridge inverter.

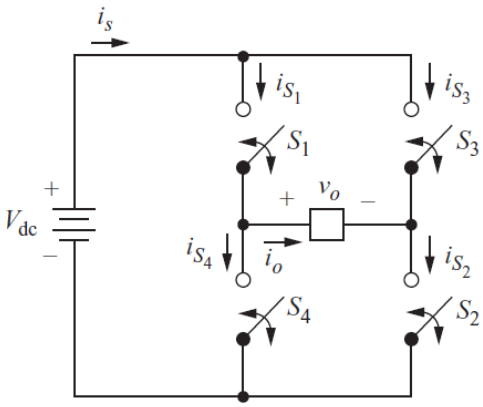

Figure 5: *Full-bridge inverter circuit* [18]

The switching combinations required to produce each voltage level are shown in Table 1. As with the half-bridge inverter, two switches in the same leg should not be in the on-state simultaneously to avoid a switch-through fault. The RMS value of the fundamental component of the output voltage with the full-bridge topology is calculated as

$$V_{1_{\mathrm{RMS}}} = \frac{1}{\sqrt{2}} \frac{4V_{\mathrm{DC}}}{\pi} = 0.9V_{\mathrm{DC}}. \tag{4}$$

As can be seen from (4), the RMS value of the output voltage is double that of the half-bridge inverter for the same DC input voltage.

Table 1: *Full-bridge inverter switching combinations*

On state	Output voltage (v_o)
S_1 and S_2	+V_{DC}
S_3 and S_4	-V_{DC}
S_1 and S_3	0 V
S_2 and S_4	0 V

Figure 6 shows the output voltage of the full-bridge inverter with square wave modulation. It can be seen that the output voltage is twice that of the half-bridge inverter which is one of the main advantages of this topology.

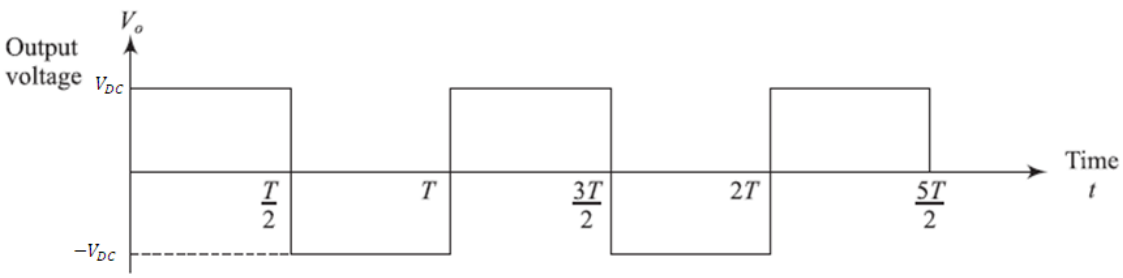

Figure 6: *Output voltage of full-bridge inverter* [20]

2.1.3 Harmonics

Within AC power systems, the term 'harmonics' refers to sinusoidal components of a periodic waveform with frequencies equal to an integer multiple of the fundamental frequency of the system [21]. The frequency (f_n) at which a specific harmonic component occurs can be calculated as

$$f_n = n \times f_{\text{fundamental}} , \tag{5}$$

where n is the harmonic order. A pure sine wave consists only of the fundamental frequency with no additional harmonic components. The existence of harmonic voltages and currents in power systems is undesirable since it leads to power quality issues such as light flickering, unwanted operation of protection equipment and overheating of transformers amongst other issues. Since the output voltage of the inverter is a square

wave, it is made up of a large number of harmonic components. Figure 7 demonstrates how the square wave is the result of the addition of higher frequency sinusoids.

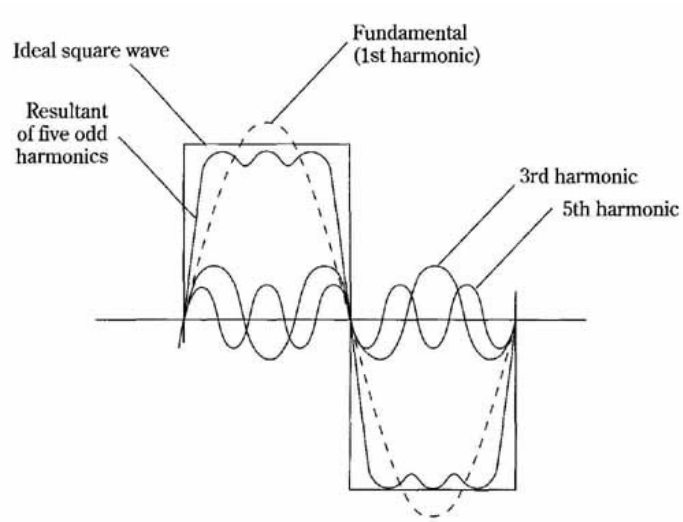

Figure 7: *Square wave and its constituent harmonic components* [22]

The RMS value of each harmonic component of the output voltage (v_n) can be calculated as

$$v_n = \frac{4V_{\mathrm{DC}}}{n\pi\sqrt{2}}\ , n = 1,2 \ldots \tag{6}$$

It can be seen from (6) that the RMS value of each harmonic component of the voltage decreases with increasing harmonic order. The lower order harmonics are the most problematic in power systems due to their higher amplitude. The quality of the output voltage or current can be expressed in terms of total harmonic distortion (THD) which can be calculated as

$$THD = \frac{\sqrt{\sum_{n=2,3,4,5\ldots}^{\infty}\left(v_{n,\mathrm{RMS}}\right)^2}}{V_{1,\mathrm{RMS}}} = \frac{\sqrt{v_{\mathrm{RMS}}^2 - V_{1,\mathrm{RMS}}^2}}{V_{1,\mathrm{RMS}}}\ . \tag{7}$$

The load current THD is calculated in the same manner, substituting voltage terms for current terms. THD may be expressed as a percentage. A low value of THD is required by IEEE 519-2014 for grid connected inverters. Low-order harmonics may be reduced by using pulse-width modulation control.

2.1.4 Pulse-width modulation control

Pulse-width modulation control is a technique used to reduce THD through the creation of a more sinusoidal inverter output voltage. The technique consists of comparing a reference signal with a high-frequency carrier signal to create gating signals for the inverter switches. There are many different types of PWM control. In this thesis, only sinusoidal PWM (SPWM) control is considered. Compared to the square wave modulation technique, where only frequency can be controlled, PWM control has the advantage of being able to control both the amplitude and frequency of the fundamental output voltage. The reduction in THD comes from the fact that low order harmonics are eliminated and due to half-wave symmetry in the output voltage, even harmonics are not present when the frequency modulation ratio is an odd integer [23]. The remaining high-order harmonics occur at the switching frequency (f_{sw}) and its sidebands and can be more easily filtered. Figure 8 shows the basic SPWM signals, with the sinusoidal reference signal (v_{control}) and the triangular carrier signal (v_{tri}).

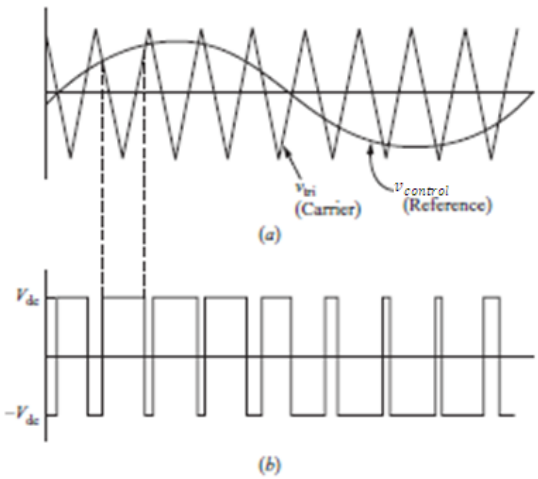

Figure 8: *PWM signals and output voltage for bipolar switching* [18]

The ratio between the amplitudes of the reference and carrier signal is known as the amplitude modulation ratio (m_{a})

$$m_{\mathrm{a}} = \frac{v_{\mathrm{tri}}}{v_{\mathrm{control}}} \ . \tag{8}$$

This ratio can be used to control the amplitude of the output voltage, with the output voltage increasing linearly until $m_{\mathrm{a}} = 1$. The ratio between the frequencies of the reference (f_{control}) and carrier (f_{tri}) signals is known as the frequency modulation ratio (m_f)

$$m_{\mathrm{f}} = \frac{f_{\mathrm{tri}}}{f_{\mathrm{control}}} \ . \tag{9}$$

The frequency of f_{control} determines the fundamental frequency of the output voltage, whilst the frequency of f_{tri} determines the switching frequency of the inverter. The frequency at which the output voltage harmonics occur can be determined by

$$f_n = (jm_{\mathrm{f}} \pm k) f_{\mathrm{fundamental}} \ , \tag{10}$$

where j and k are integer numbers. If j is odd, then k must be even and vice versa. For values of j above 4, the amplitude of the harmonic components become negligible [24]. The harmonic order n is found from

$$n = jm_{\mathrm{f}} \pm k \ , \tag{11}$$

with the fundamental frequency corresponding to n=1. The amplitudes of the harmonic components can be found using Fourier analysis.

2.1.5 Bipolar modulation

Bipolar modulation is a method of SPWM where a single sinusoidal reference signal is compared with a high-frequency carrier signal to produce gating signals for the switches in the inverter circuit. Figure 8 shows the reference and carrier signals for the bipolar switching scheme and the resultant output voltage waveform. When the amplitude of the reference signal is greater than the carrier signal, the output voltage is equal to $+V_{\mathrm{DC}}$, and when it is smaller than the carrier signal, the output voltage is equal to $-V_{\mathrm{DC}}$. The largest amplitude harmonics occur at the switching frequency and its sidebands. With reference to the full-bridge circuit in Figure 5, the on and off-states of the switches are:

$$v_{\mathrm{control}} > v_{\mathrm{tri}}, \qquad s_1 \text{ and } s_2\text{: on}$$
$$v_{\mathrm{control}} < v_{\mathrm{tri}}, \qquad s_3 \text{ and } s_4\text{: on}$$

2.1.6 Unipolar modulation

Unipolar modulation is similar to bipolar modulation with the difference being that two sinusoidal reference signals are used instead of one. The second reference signal is 180º out of phase with the first. This results in three different levels of output voltage – V_{DC}, $-V_{\mathrm{DC}}$, and 0 V. Figure 9 shows the reference and carrier signals for unipolar switching and the resultant output voltage waveform.

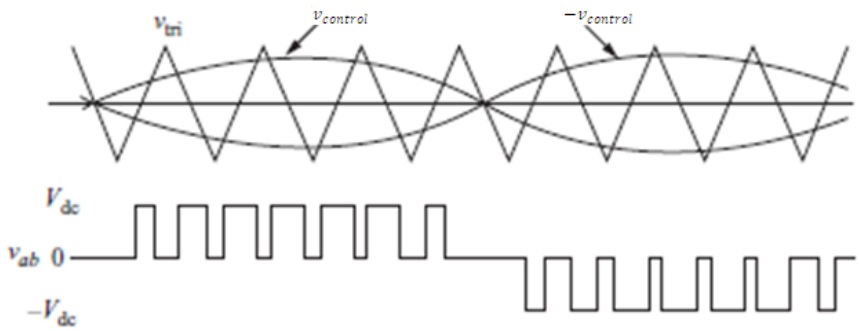

Figure 9: *PWM signals and output voltage for unipolar switching* [18]

The advantage of the unipolar switching scheme is that the switching frequency is effectively doubled, and the largest amplitude harmonics occur at $2m_{\mathrm{f}}$ and its sidebands. It can be noted also that the steps in the output voltage amplitude are reduced to 0 and $\pm V_{\mathrm{DC}}$ compared to $\pm 2V_{\mathrm{DC}}$ for the bipolar switching scheme. For the full-bridge inverter the on and off-states of the switches are:

$$v_{\mathrm{control}} > v_{\mathrm{tri}}, \quad s_1\text{: on}$$
$$v_{\mathrm{control}} < v_{\mathrm{tri}}, \quad s_3\text{: on}$$
$$\text{-}v_{\mathrm{control}} > v_{\mathrm{tri}}, \quad s_2\text{: on}$$
$$\text{-}v_{\mathrm{control}} < v_{\mathrm{tri}}, \quad s_4\text{: on}$$

The switching combinations required to produce the output voltage levels of V_{DC}, -V_{DC} and 0 V are the same as shown in Table 1. Figure 10 shows a comparison of the inverter output voltages for the bipolar and unipolar methods. It can be seen clearly that the unipolar method produces a waveform closer to a sinusoid and therefore, with lower harmonic distortion, however, problematic harmonics still exist. These can be further attenuated by the use of a filter inductor. Figure 11 shows the improvement in the quality of the voltage that can be achieved through filtering.

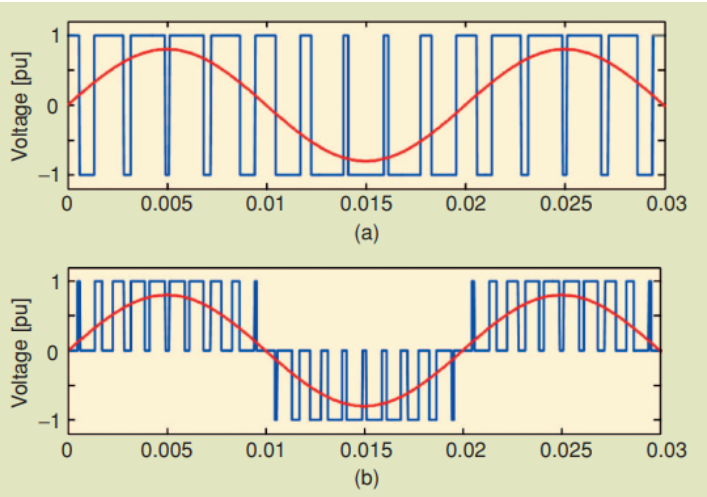

Figure 10: *(a) Bipolar inverter output (b) Unipolar inverter output* [25]

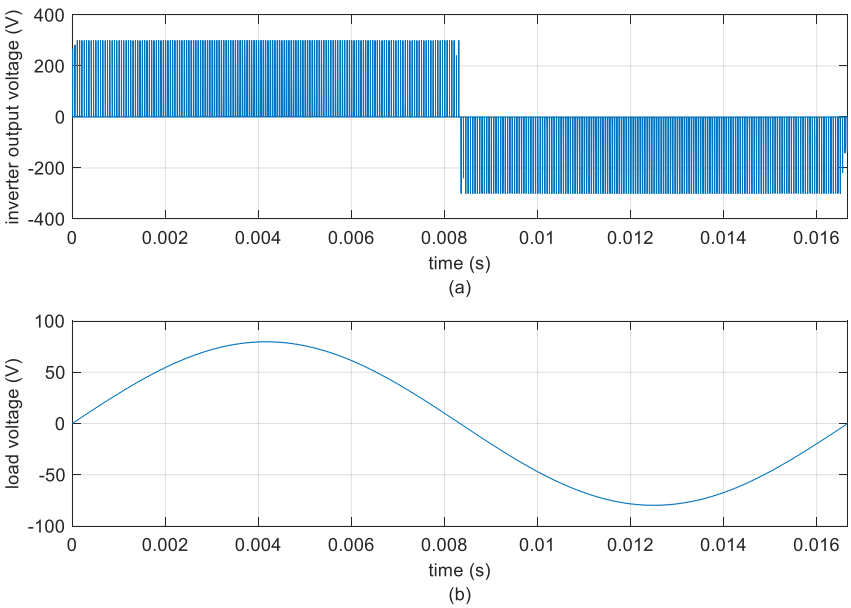

Figure 11: *(a) PWM inverter output voltage (b) Load voltage after filtering*

2.2 Filter inductors

The L-filter is a type of low pass filter which attenuates frequencies above a certain value known as the cut-off frequency. This is especially useful in reducing the harmonics produced by PWM inverters. For the elimination of switching ripple in the output current, a filter with a low cut-off frequency and high attenuation at the switching frequency is needed [26]. Traditionally, the L-filter was used as an interface between converters and the grid, however LCL-filters are more commonly used now due to better efficiency and lower cost and volume [27], [28]. In this thesis the L-filter is considered for simplicity and to keep the focus on inductor design. The methods used in this thesis can be adapted for the design of other types of filter. Figure 12 shows the filter inductor at the output of a full-bridge inverter with a resistive load.

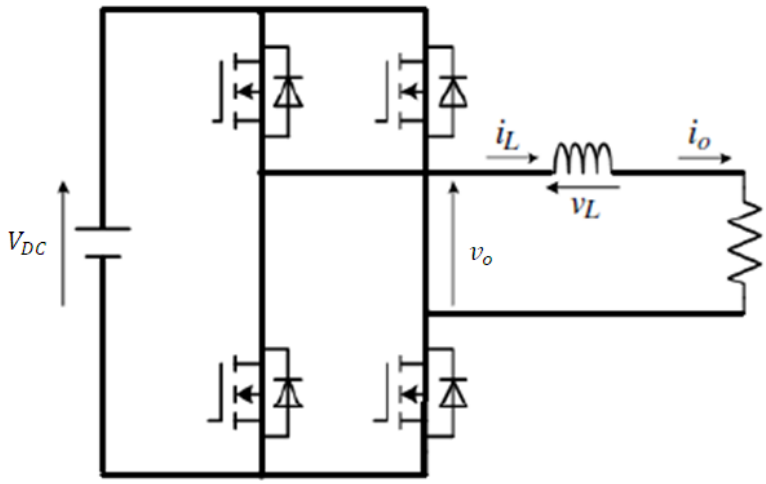

Figure 12: *Full-bridge inverter with L-filter* [29]

Figure 13 shows the output current ($i(t)$) of an inverter. It can be seen that there are high frequency variations in the output current compared to the fundamental frequency. This is known as switching ripple and is due to the high-order harmonic content in the output current. The magnitude of the peak-to-peak variations can be reduced by increasing the switching frequency but since this increases switching losses, a better option is to use a filter inductor. The inductor works by opposing rapid changes in the current through it.

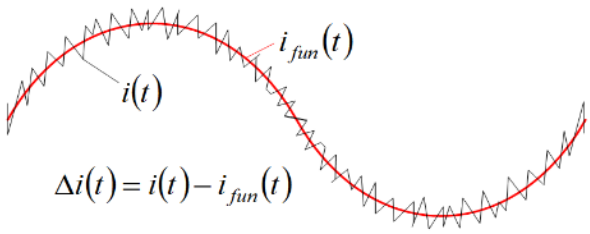

Figure 13: *Inverter output current* [30]

The maximum peak-to-peak ripple current is found from

$$\Delta i_{\mathrm{pp,max}} = \frac{V_{\mathrm{DC}} T_{\mathrm{s}}}{4 L_{\mathrm{ref}}}, \tag{12}$$

where V_{DC} is the DC input voltage and $T_{\mathrm{s}} = \frac{1}{f_{\mathrm{sw}}}$ is the switching time. The inductance (L_{ref}) required to tolerate this ripple is found from

$$L_{\mathrm{ref}} = \frac{V_{\mathrm{DC}}}{4 f_{\mathrm{sw}} \Delta i_{\mathrm{pp}}|_{\mathrm{max}}}. \tag{13}$$

Therefore, when the value of the output current is known, the required inductance value to limit the ripple in the output current can be calculated.

2.2.1 Electromagnetic principles

Figure 14 shows a current-carrying conductor. When current is flowing through the conductor, a magnetic field is induced around it [31]. The magnetic field is described by magnetomotive force (MMF) ($\mathcal{F}$), magnetic field intensity ($\boldsymbol{H}$), magnetic flux density ($\boldsymbol{B}$), magnetic flux (Φ), and magnetic flux linkage (λ) [32].

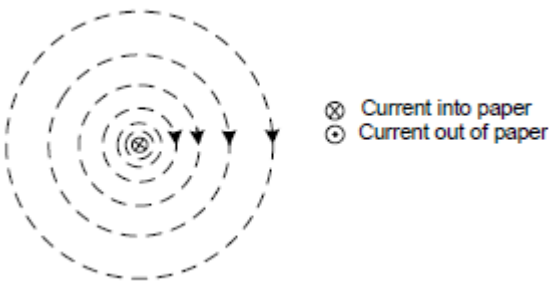

Figure 14: *Magnetic field around a current-carrying conductor* [31]

An inductor consists of a current-carrying conductor coiled into a winding with N turns. When there is current in the winding, MMF is produced. The coil is often wound around a core of ferromagnetic material to increase inductance as in Figure 15.

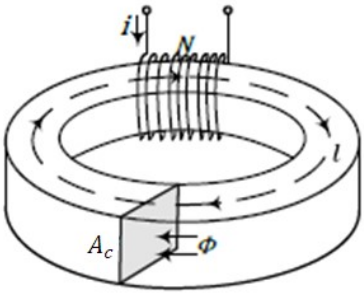

Figure 15: *Current-carrying conductor wound around ferromagnetic core* [33]

MMF in the magnetic circuit is analogous to electromotive force in the electrical circuit and is the potential difference between any two points [32]. In magnetic circuits, MMF is a source and causes flux to flow. The magnetomotive force is calculated as

$$\mathcal{F} = Ni\,, \tag{14}$$

where N is the number of winding turns and i is the current through the conductor. The MMF produces the magnetic field, the intensity of which can be calculated as

$$H = \frac{\mathcal{F}}{l_c} = \frac{Ni}{l_c}\,, \tag{15}$$

where l_c is the magnetic path length. It can be seen from (15) that H is directly proportional to the current and the number of turns per unit length. H can also be expressed as

$$H = \frac{i}{2\pi r}, \tag{16}$$

where r is the radial distance from the centre of the conductor. The magnetic flux passing through an open surface S is given by

$$\Phi = \int_S \boldsymbol{B} \cdot d\boldsymbol{S}\,, \tag{17}$$

where $\boldsymbol{B}$ is the magnetic flux density.

If the magnetic flux density is uniform and perpendicular to the surface $\boldsymbol{S}$, then the magnetic flux can be given by [31], [32]

$$\Phi = BA_{\mathrm{c}}, \tag{18}$$

where A_c is the cross-sectional area of the surface. From (18) it can be seen that, for an inductor, the magnetic flux can be increased by increasing the surface area of a winding turn [32]. From (18) it can also be seen that flux density is the total flux divided by the cross-sectional area through which it flows. Flux density is related to magnetic field strength through

$$\boldsymbol{B} = \mu \boldsymbol{H}\,, \tag{19}$$

where μ is the permeability. Permeability refers to the ability of a material to conduct flux [34] and can be written as

$$\mu = \mu_0 \mu_{\mathrm{r}}\,. \tag{20}$$

$\mu_0 = 4\pi \times 10^{-7}$ H/m is the permeability of free space. μ_{r} is the relative permeability of a material (relative to free space). Using a core with a high permeability can reduce the number of winding turns required to produce a given inductance. When a time-varying current is present, a time-varying magnetic field is produced. Time-varying magnetic flux passing through a closed loop induces a voltage in that loop [31]. This is the basis of Faraday's law

$$v(t) = \frac{d\Phi(t)}{dt}. \tag{21}$$

For an inductor with N turns, the voltage across the inductor will be

$$v(t) = N\frac{d\Phi(t)}{dt} = \frac{d\lambda(t)}{dt}, \tag{22}$$

where λ is flux linkage. Flux linkage is the sum of the flux enclosed by each winding turn of an inductor. Figure 16 shows the lines of flux through the winding turns.

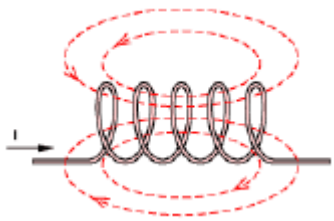

Figure 16: *Flux linked by coils* [35]

For uniform flux density, λ is given by

$$\lambda = N\Phi = NA_{\mathrm{c}}B = NA_{\mathrm{c}}\mu H = \frac{\mu A_{\mathrm{c}}N^2 i}{l_{\mathrm{c}}} = Li\,, \tag{23}$$

where L is the inductance of the winding. Inductance is the measure of a coil's ability to store energy in the form of a magnetic field [35]. The differential inductance is defined as the rate of change of flux with current

$$L(i) = \frac{d\Phi}{di} = \frac{N^2 A_{\mathrm{c}}}{l_{\mathrm{c}}}\mu_{\mathrm{d}}(H)\,, \tag{24}$$

where μ_{d} is the differential permeability and describes the relationship between the magnetic field strength H and the flux density B and is dependent on the core material [36].

$$\mu_{\mathrm{d}}(H) = \frac{dB}{dH} \tag{25}$$

2.2.2 Materials

Materials can be classified as diamagnetic, paramagnetic or ferromagnetic. For diamagnetic and paramagnetic materials, the value of relative permeability is close to 1. The diamagnetic material has a permeability which is slightly less than that of free space, meaning that it slightly opposes a magnetic field. The paramagnetic material has a relative permeability slightly higher than that of free space meaning that slight magnetisation occurs when a magnetic field is applied [31]. In contrast, ferromagnetic materials have high relative permeabilities and readily support the formation of magnetic fields. Since the purpose of magnetic cores is to concentrate the magnetic field in the core, and to provide a low reluctance path for magnetic flux, ferromagnetic materials

are used to make cores. Ferromagnetic materials can be described as hard or soft, with soft magnetic materials being easily magnetised and demagnetised which makes them suitable for use in inductor and transformer applications. It is difficult to magnetise and demagnetise hard magnetic materials and they are often used as permanent magnets [32]. A common soft magnetic material used in magnetic cores is silicon steel – an iron alloy with good magnetic properties made from iron and a small percentage of silicon. The addition of silicon improves the magnetic properties of the material and increases resistivity leading to a reduction in eddy current losses.

2.2.3 Losses in inductors

Power losses are inherent in magnetic components. For inductors, the losses can be categorised as winding losses and core losses. These losses are dissipated as heat. Figure 17 shows how the main losses may be classified in inductors.

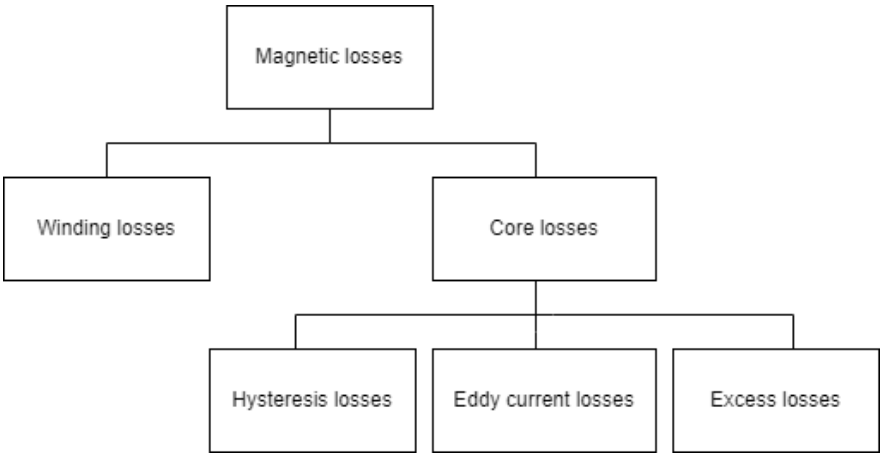

Figure 17: *Classification of losses in magnetic components*

The winding losses may be further divided into losses related to DC resistance and AC resistance which includes the skin effect and the proximity effect. For a DC current, only copper losses exist, without frequency all other losses are reduced to zero. Core losses consist of hysteresis losses, eddy current losses, and excess or anomalous losses which refers to losses related to complex mechanisms in the magnetisation process not explained by hysteresis or eddy current losses [31], [37]. Careful consideration of winding and core losses is important when designing magnetic components. Total losses in the inductor can be written as

$$P_{\text{total}} = P_{\text{winding}} + P_{\text{core}} \,, \tag{26}$$

where

$$P_{\mathrm{core}} = P_{\mathrm{hy}} + P_{\mathrm{cl}} + P_{\mathrm{ex}} \,. \tag{27}$$

P_{hy} is the hysteresis losses, P_{cl} the eddy current losses, and P_{ex} the excess losses.

2.2.4 Winding losses

The winding of the inductor has a DC resistance R_{DC} which opposes the flow of current. This resistance leads to power losses in the form of heat. The DC resistance of a conductor of length l_{Cu}, cross-sectional area A_{Cu}, and resistivity ρ is given by

$$R_{\mathrm{DC}} = \rho \frac{l_{\mathrm{Cu}}}{A_{\mathrm{Cu}}} . \tag{28}$$

Typically, copper is used in inductor windings since it is a good conductor with a low value of resistivity. The resistive losses in the inductor for DC current flow can be calculated by

$$P_{\mathrm{DC}} = R_{\mathrm{DC}} i_{\mathrm{DC}}^2 , \tag{29}$$

where i_{DC} is the DC component of the current through the inductor. In PWM converter applications, the inductor current contains a DC component, a fundamental component and harmonic components since the current is non-sinusoidal [38]. The resistance of the winding conductor increases with frequency due to skin and proximity effects. The AC resistance is found from Dowell's equation and can be approximated as [39]

$$R_{\mathrm{AC}} = R_{\mathrm{DC}} A_0 \left(1 + \frac{2\left(N_{\mathrm{l}}^2 - 1\right)}{3} \right) , \tag{30}$$

where A_0 is a dimensionless quantity dependent on the conductor geometry [40] which takes into account the skin effect at the operating frequency and N_{l} is the number of winding layers. The AC-to-DC winding resistance ratio can be written as

$$F_{\mathrm{R}} = \frac{R_{\mathrm{AC}}}{R_{\mathrm{DC}}} \,. \tag{31}$$

The AC winding losses are then found from

$$P_{\mathrm{AC}} = F_{\mathrm{R}} P_{\mathrm{DC}} \tag{32}$$

Current is distributed uniformly throughout the cross-section of the winding conductor at DC and low frequencies. The current density in the conductor is found from

$$J_{\mathrm{m}} = \frac{I_{\mathrm{m}}}{A_{\mathrm{Cu}}}. \tag{33}$$

As frequency increases, the current in the conductor becomes distributed closer to the surface or *skin* of the conductor. This is because eddy currents are generated in the conductor which force the current to the surface as shown in Figure 18. This phenomenon effectively reduces the cross-sectional area of the conductor, thereby increasing resistance and resistive losses.

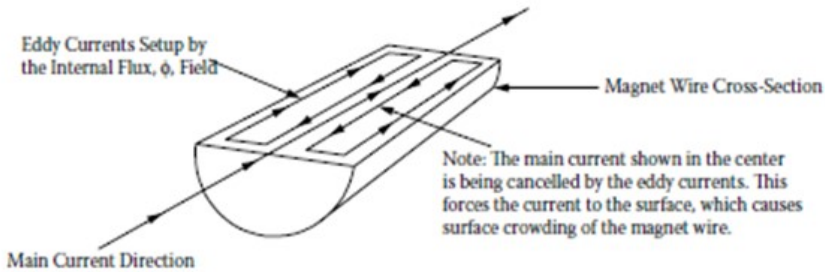

Figure 18: *Skin effect in a conductor* [34]

The skin depth is the depth at which 63% of the current resides in the conductor

$$\delta = \sqrt{\frac{\rho}{\pi \mu_0 f}}, \tag{34}$$

where f is frequency and ρ is the resistivity of the conductor. It can be seen from (34) that the skin depth decreases as the frequency increases. Figure 19 shows how the current can be concentrated near the surface of the conductor due to the skin effect.

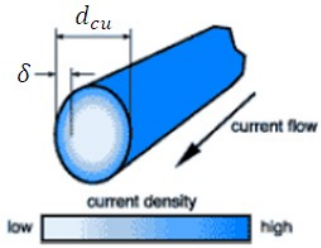

Figure 19: *Current density in a conductor due to the skin effect* [35]

Another phenomenon occurring in conductors is the proximity effect. The proximity effect, like the skin effect, is more pronounced at higher frequencies, reduces the effective cross-sectional area of the conductor and affects the distribution of the current in the conductor. Eddy currents can be induced in a conductor by the alternating magnetic field of nearby inductors. This is important to consider for inductors since the winding turns are adjacent to each other and often layered on top of each other. Reducing the number of winding layers or turns in an inductor can reduce problems caused by the proximity effect. Figure 20 shows how the proximity effect affects current density and distribution for different directions of current flow in adjacent conductors.

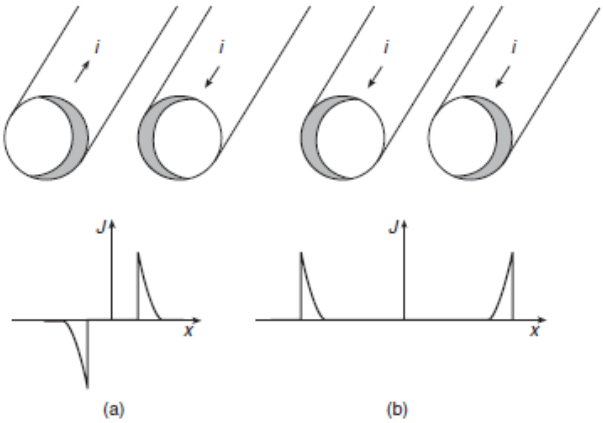

Figure 20: *Current distribution in adjacent conductors due to the proximity effect* [32]

2.2.5 Core losses

In addition to losses that occur in the inductor windings, losses also occur in the inductor core in the form of hysteresis losses, eddy current losses and excess losses. The inductor core exists to concentrate the magnetic field within the core and to provide an easy path for magnetic flux [32].

Hysteresis losses refer to losses that occur due to the hysteresis phenomenon in magnetic materials. With reference to Figure 21, when a demagnetized material is exposed to a magnetic field, the flux density (B) in the material begins to increase as the field strength (H) is increased and follows path (a). When the flux density reaches B_{sat}, further increase in the magnetic field strength do not yield further increases in flux density. When the field strength is then reduced back to zero, the flux density in the material does not reduce back to zero, instead following path (c) and a remanent flux (B_{r}) remains in the material. In order to reduce the flux density back to zero, a negative value of H is required. This negative force is known as the coercive force (H_{c}). Continuously decreasing H_{c} leads to saturation at -B_{sat}, where further decreasing H yields no changes in B. Upon returning H to zero, B does not return to zero but to -B_{r}. Increasing H once more causes the flux density now to follow path (b) since the magnetisation is only partially reversible [32]. Now cycling H will cause B to follow the outer loop of the graph in Figure 21. This loop is known as the hysteresis loop.

The hysteresis effect can be attributed to the impedance of magnetisation caused by domain wall pinning [41]. Within ferromagnetic materials, there exists magnetic domains. Within the magnetic domains, the magnetic moments are oriented in the same direction, but this direction varies from domain to domain when the material is in a demagnetised state. When a magnetic field is applied the magnetic moments align with the direction of the applied field. Separating each domain are domain walls which move when a magnetic field is applied. The movement of the domain walls is impeded by the existence of pinning sites in the material. The pinning sites are regions in the material which contain non-magnetic inclusions [42]. The pinning sites are caused by impurities in the material. Energy is required to move domain walls across pinning sites [43].

For one cycle of the hysteresis loop, the energy lost due to the hysteresis effect can be measured as the area inside the loop. Since energy is lost each cycle, hysteresis power losses increase with frequency. The hysteresis loop depends on the properties of the material and for non-magnetic materials, the B-H curve is linear as shown by path (d) in Figure 21.

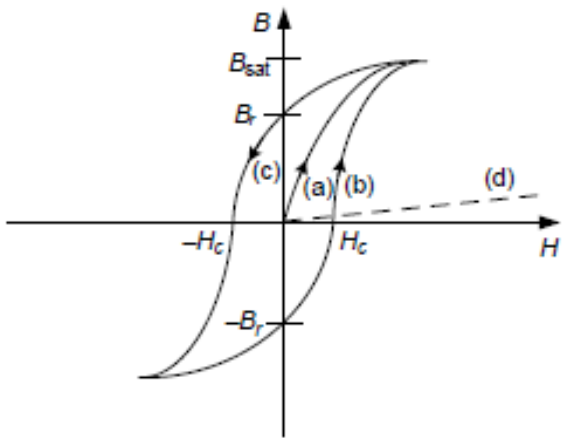

Figure 21: *B-H magnetisation curve* [14]

Hysteresis losses per unit volume for sinusoidal current excitation can be found from the Steinmetz empirical equation

$$p_{\mathrm{h}} = k_{\mathrm{h}} f^{\alpha} B_{\mathrm{m}}^{\beta}, \tag{35}$$

where k_{h}, α and, β are empirical constants dependent on the material, and B_{m} is the maximum value of flux density.

Inductor cores are typically made from conducting materials and are therefore susceptible to the formation of eddy currents inside them as a result of Faraday's law described by (21). The eddy currents in the core give rise to resistive losses in the form of heat due to the internal resistance of the core material. Eddy current losses increase with frequency. In order to combat eddy current losses, cores are often made from thin laminations stacked together instead of a single solid block. Magnetic flux is able to travel through the laminations, but since the laminations are coated in an insulating material, currents are confined. Making the core from laminations increases the overall resistance of the core, thereby reducing the eddy currents. The sum of the eddy currents flowing in each lamination is smaller than the eddy currents flowing in the equivalent solid core.

The skin effect is also present in magnetic cores. The effect causes the magnetic flux to be concentrated at the surface of the core with little flux in the centre for a solid core meaning that the reluctance of the core is increased and the ability to provide a low reluctance path for flux is decreased [31]. For grain-oriented silicon steel, the skin depth is around 0.5 mm at 50 Hz [14]. For a 0.5 mm lamination, the distance from the surface

to the centre is half a skin depth and the flux can be assumed to be uniform within it [44]. Figure 22 shows the circulation of eddy currents in the solid core and in the laminated core.

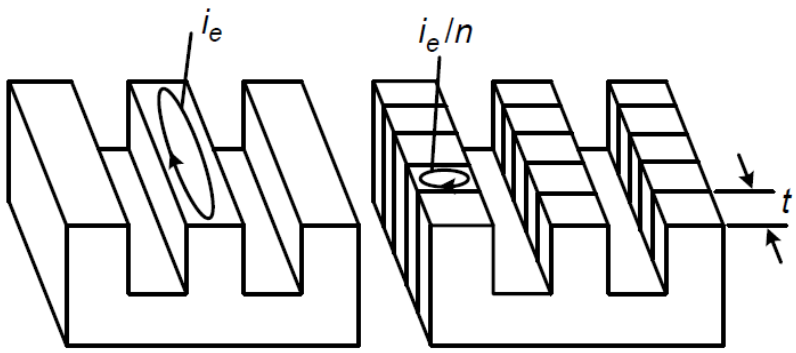

Figure 22: *Eddy currents in solid and laminated cores* [14]

The general form of the equation for eddy current losses is

$$p_{\mathrm{e}} = k_{\mathrm{e}} f^2 B_{\mathrm{m}}^2 \,, \tag{36}$$

where k_{e} is an experimentally determined coefficient and is proportional to the square of the lamination thickness.

The final category of core losses is termed anomalous or excess losses, these losses can be observed in measurements and are not explained by the equations for hysteresis and eddy current losses. Excess losses are attributed to complex mechanisms in the magnetisation process and are result of the existence of magnetic domains [31]. The excess loss term in (27) can be approximated as

$$p_{\mathrm{ex}} \sim C(f B_{\mathrm{m}})^{\frac{3}{2}} \,, \tag{37}$$

where C is a coefficient that depends on the shape and material of the core.

3. DESIGN AND SIMULATION METHODS

This chapter presents a design method for quickly designing toroidal filter inductors based on the area-product method. A simulation model for analysing the behaviour of the designed inductors is also described.

3.1 Area-product design method

When designing inductors, electrical, mechanical, and thermal requirements should be taken into consideration. One well-established method for inductor design which takes into account these considerations is the area-product method. Once the desired inductance value L_{ref}, maximum current I_{m}, current density J_{m}, and maximum flux density B_{m} have been chosen, the area-product method follows a step-by-step process to provide a suitable core and winding arrangement for the inductor. The area-product method is so called because it is the product of the cross-sectional area (A_{c}) of the core and the core winding window area (W_{a}). Rearranging (23), it can be seen that the required cross-sectional area of the core for a given inductance is

$$A_{\mathrm{c}} = \frac{L_{\mathrm{ref}} I_{\mathrm{m}}}{N B_{\mathrm{m}}} \ . \tag{38}$$

The number of turns required for the inductance is found from

$$N = \frac{J_{\mathrm{m}} k_{\mathrm{u}} W_{\mathrm{a}}}{I_{\mathrm{m}}} \ , \tag{39}$$

where k_{u} is the winding window utilisation factor. Rearranging (39), the winding window area can be determined from

$$W_{\mathrm{a}} = \frac{N I_{\mathrm{m}}}{J_{\mathrm{m}} k_{\mathrm{u}}} \ . \tag{40}$$

Multiplying (38) and (40), the area-product A_p is then found from

$$A_\mathrm{p} = W_\mathrm{a} A_\mathrm{c} = \frac{L_\mathrm{ref} I_\mathrm{m}^2}{k_\mathrm{u} J_\mathrm{m} B_\mathrm{m}} \ , \tag{41}$$

It may be noted that for the same area-product there can be any number of different core geometries so long as A_p= $W_\mathrm{a} A_\mathrm{c}$. Figure 23 shows how the core cross-section and winding window area are related to the geometry of a toroidal inductor.

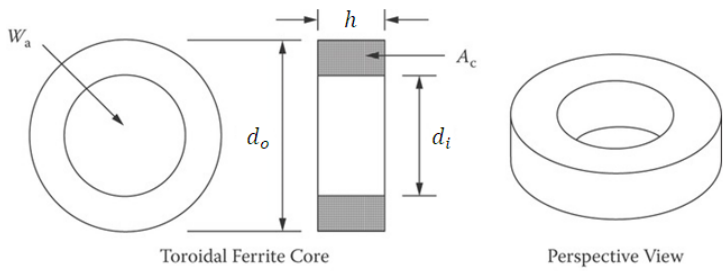

Figure 23: *Winding window area and core cross-section of toroidal core* [34]

The parameter k_u is a measure of how much of the winding window area is filled by the copper of the winding inductor. k_u is unitless and is found from

$$k_\mathrm{u} = k_1 k_2 k_3 k_4, \tag{42}$$

where k_1 is the ratio of the area of the bare winding wire to the area of the insulated winding wire, k_2 is the fill factor – which accounts for the space found between winding turns and layers – k_3 is the effective window which defines how much of the winding window may actually be used for the winding [34] since often coil formers are used for the windings which take up space in the winding window, or in the case of toroids, space must be left for a winding shuttle to pass through. k_4 is the insulation factor which accounts for the space taken up in the window area by tape insulation used between winding layers and as wrapping. These factors may be individually calculated as described in [34] to determine a value for k_u, however 0.4 is usually selected as an appropriate value. In toroidal inductors k_u may be as low as 0.15-0.25 to allow for the winding shuttle to pass through the window area [32].

Once the area-product has been determined from (41), the next step is to select the closest core from standard core sizes which has the same area-product as the calculated area-product. Since it is unlikely an off-the-shelf core will match exactly the calculated area-product, the core selected must be slightly larger than required in order to meet the design requirements and prevent unwanted effects such as core saturation that could occur from selecting a core with a smaller area-product than that calculated. Using larger than necessary cores adds unnecessary size and weight to the finished inductor which is an issue if the intention is to produce as compact and lightweight inductors as possible. Methods for rapidly designing large numbers of geometrically unique inductors which match the area-product exactly and which can be quickly modelled and prototyped offer a possible solution and are discussed in the next section.

Once a suitable core has been selected, the next step in the process is the winding design. The available window area based on the selected core can be found by

$$W_{\mathrm{a}} = \frac{A_{\mathrm{p}}}{A_{\mathrm{c}}}. \tag{43}$$

The number of turns required in the winding is found by

$$N = \frac{k_{\mathrm{u}} W_{\mathrm{a}}}{A_{\mathrm{Cu}}}, \tag{44}$$

where A_{Cu} is the cross-sectional area of the winding conductor and is found from rearranging (33)

$$A_{\mathrm{Cu}} = \frac{I_{\mathrm{m}}}{J_{\mathrm{m}}}. \tag{45}$$

Once the number of winding turns has been determined, the next step in the process is determining the correct length of the air gap in the core. The air gap increases the amount of current required to drive the core into saturation. Determining the air gap length is an iterative process and involves also determining the fringing-flux factor.

Whenever the core is excited, fringing flux is present around the air gap [32] as shown in Figure 24.

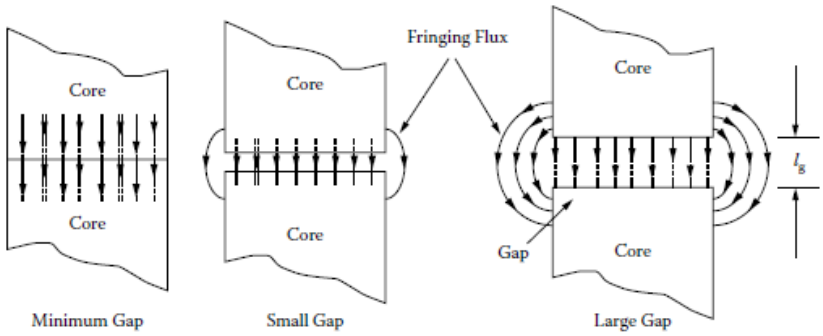

Figure 24: *Fringing flux around air gaps of different sizes* [34]

The fringing phenomenon occurs because the lines of flux repel each other when passing through non-magnetic materials [45]. As a consequence, the cross-sectional area of the magnetic field is increased, decreasing the flux density. Fringing flux typically effectively increases the air gap cross-sectional area by 10 % and the radius of fringing flux is approximately equal to the air gap length. Fringing flux can lead to losses, inducing eddy currents in the windings in the vicinity of the air gap leading to intense localised heating. When winding inductors, winding over the air gap should be avoided to prevent the fringing flux inducing eddy currents in the conductor. To account for the fringing effect, a fringing factor is used when determining the length of the air gap. Initially, the air gap length is found by

$$l_{\mathrm{g}} = \frac{\mu_0 A_{\mathrm{c}} N^2}{L_{\mathrm{ref}}} - \frac{l_{\mathrm{c}}}{\mu_{\mathrm{r}}}, \tag{46}$$

where l_{c} is the mean magnetic path length and μ_{r} the relative permeability of the selected core material. Once the air gap length is determined, the fringing flux factor (F_{f}) is determined. The reluctance of the toroidal core is found from

$$\mathcal{R}_{\mathrm{core}} = \left(\frac{\mu h}{2\pi} \ln \frac{d_{\mathrm{o}}}{d_{\mathrm{i}}}\right)^{-1}, \tag{47}$$

Where d_{o} and d_{i} are the outer and inner diameters of the toroid respectively. Magnetic reluctance is a measure of the opposition of the flow of magnetic flux. It is analogous to resistance in electrical circuits. The reluctance of the air gap is very high and is found by

$$\mathcal{R}_{\mathrm{gap}} = \frac{l_{\mathrm{g}}}{\mu_0 A_{\mathrm{c}}}. \tag{48}$$

Taking into account the fringing effect, the reluctance of the air gap is found by

$$\mathcal{R}_{\mathrm{gap,f}} = \frac{l_{\mathrm{g}}}{\mu_0 A_{\mathrm{c}} F_{\mathrm{f}}}. \tag{49}$$

The total reluctance taking into account the fringing effect is

$$\mathcal{R}_{\mathrm{total}} = \mathcal{R}_{\mathrm{core}} + \mathcal{R}_{\mathrm{gap,f}}\,. \tag{50}$$

The inductance taking into account the fringing effect is found from

$$L_{\mathrm{ref}} = \frac{N^2}{\mathcal{R}_{\mathrm{total}}} = \frac{\mu_0 N^2}{\left(\dfrac{2\pi}{\mu h \ln \dfrac{d_o}{d_{\mathrm{i}}}} + \dfrac{l_{\mathrm{g}}}{A_{\mathrm{c}} F_{\mathrm{f}}}\right)}\,. \tag{51}$$

Rearranging (51), the fringing flux factor can be found from

$$F_{\mathrm{f}} = \frac{l_{\mathrm{g}}}{A_{\mathrm{c}}\left(\dfrac{\mu_0 N^2}{L_{\mathrm{ref}}} - \dfrac{2\pi}{\mu h \ln \dfrac{d_{\mathrm{o}}}{d_{\mathrm{i}}}}\right)}\,. \tag{52}$$

Now that the fringing flux factor has been determined, a new value for the air gap length is determined from

$$l_{\mathrm{g}} = \frac{\mu_0 A_{\mathrm{c}} F_{\mathrm{f}}}{L_{\mathrm{ref}}}\left(N^2 - \frac{L_{\mathrm{ref}} l_{\mathrm{c}}}{\mu_0 \mu_{\mathrm{r}} A_{\mathrm{c}}}\right). \tag{53}$$

The final step is to carry out iterative calculations between (52) and (53) until convergence of l_{g} and F_{f}, leaving the final calculated value for the air gap length.

The steps in the design process can be summarised as:

1. Calculate area-product based on inductor requirements (L_{ref}, B_{m}, J_{m}, I_{m}, and k_{u}).
2. Select core with area-product closest to the calculated value, always choosing larger rather than smaller.
3. Calculate size of window area (W_{a}).
4. Calculate required number of turns (N).
5. Calculate the air gap length (l_{g}).
6. Calculate the fringing flux factor (F_{f}).
7. Iterate until convergence for air gap length and fringing flux factor to find final value for air gap length.

3.2 Filter inductor design procedure

As discussed previously, filter inductors are needed at the output of inverters to reduce the harmonics created by the PWM control of the inverter switches. The filters designed in this thesis are designed to keep the switching ripple in the output current below 5 %. A script was written in MATLAB which created 300 different toroidal core geometries by varying the area of the core cross-section and as a result the winding window area. The different core cross-sectional areas were created by changing the parameters k_{d} and h. k_{d} refers to the ratio between the outer diameter and inner diameter of the toroidal core ($k_{\mathrm{d}} = \frac{d_{\mathrm{o}}}{d_{\mathrm{i}}}$), and h to the toroidal core height. The core height and inner and outer diameters are shown in Figure 23. Writing the area-product for toroidal inductors in terms of k_{d}, h, and d_{i} gives

$$A_{\mathrm{p}} = W_{\mathrm{a}} A_{\mathrm{c}} = \left(\frac{d_{\mathrm{i}}^3 \pi h (k_{\mathrm{d}} - 1)}{8} \right), \tag{54}$$

where

$$A_{\mathrm{c}} = h \frac{(k_{\mathrm{d}} - 1) d_{\mathrm{i}}}{2}, \tag{55}$$

and

$$W_{\mathrm{a}} = \pi \left(\frac{d_{\mathrm{i}}}{2}\right)^2 . \tag{56}$$

Rearranging (54), the inner diameters for the designs can then be found from

$$d_{\mathrm{i}} = \left(\frac{8A_{\mathrm{p}}}{\pi h(k_{\mathrm{d}} - 1)}\right)^{\frac{1}{3}} , \tag{57}$$

and the outer diameters from

$$d_{\mathrm{o}} = k_{\mathrm{d}} d_{\mathrm{i}} . \tag{58}$$

Once the inductor core cross-sectional areas are calculated, the design process proceeds in the same way as for the area-product method described in Section 3.1. The winding window area is calculated, the number of turns are calculated and the air gap length is calculated. The cores are made from M330-35A non-grain-oriented silicon steel laminations having a relative permeability of 7650 and lamination thickness 0.35 mm. The B-H curve for M330-35A is shown in Figure 25. The MATLAB script used to create the inductor designs is shown in Appendix A. COMSOL Multiphysics finite element analysis software was used to calculate the values used for the fringing flux factor and this data was used in the design process.

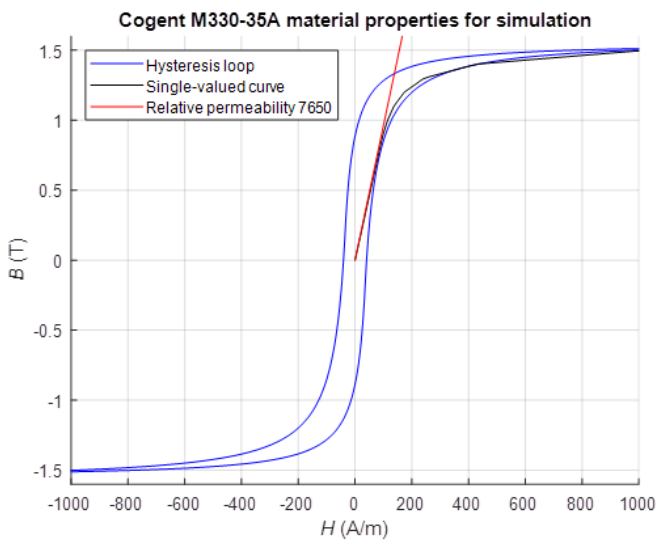

Figure 25: *B-H curve for M330-35A silicon steel*

3.3 Simulink inductor model

When the filter inductors have been designed, the next step is to simulate their behaviour using MATLAB Simulink. Simulink is a graphical environment for designing, modelling, and simulating dynamic systems using block diagrams. The blocks represent different components in the system and can be taken from pre-existing blocks in the Simulink library or can be user defined. The Simulink model used is based on that in [46] which models core losses using the principle of loss separation, where each component of the core losses is considered separately. The model takes into account the geometry and material properties of the cores developed in the previous section as well as the winding length to give an accurate estimation of the inductor losses when fed by a PWM inverter with IGBT switches and unipolar modulation. One benefit is that the behaviour of each inductor can be modelled more quickly (a matter of seconds rather than hours) and with less computational resources than with a finite element analysis method. Figure 26 shows a simplified diagram of the PWM inverter and filter inductor model. More detailed diagrams of each component of the inductor model are shown in Appendix B.

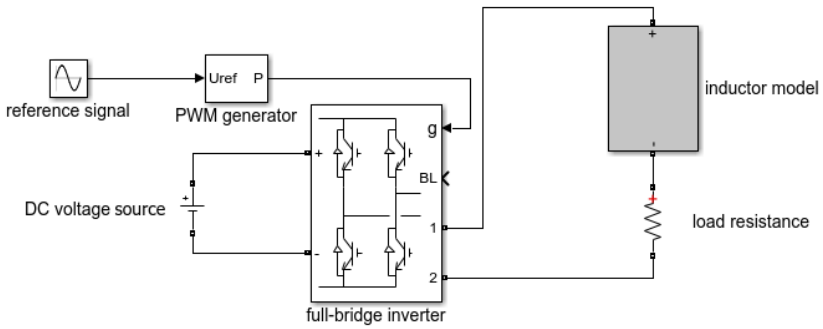

Figure 26: *MATLAB Simulink model of PWM supplied filter inductor*

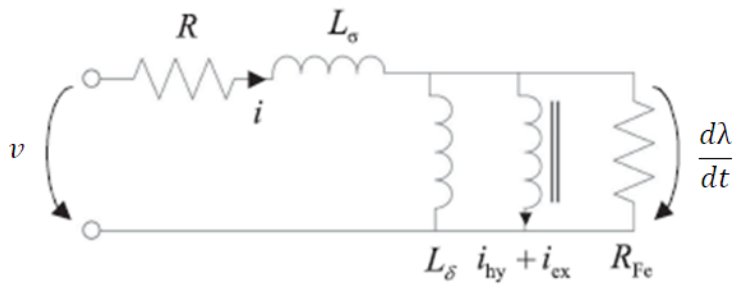

Figure 27: *Equivalent circuit of inductor with air gap* [46]

Figure 27 shows the equivalent circuit of an inductor with an air gap used in the modelling. The voltage equation for the inductor is written as

$$v = Ri + L_\sigma \frac{di}{dt} + \frac{d\lambda}{dt}, \tag{59}$$

where v is the inductor voltage, R is the inductor resistance, L_σ the leakage inductance and, λ the flux linkage. The flux linkage is related to the average flux density in the core b_0 by

$$\lambda(t) = NA_c b_0(t). \tag{60}$$

From ampere's law and neglecting fringing flux, MMF is found from

$$Ni(t) = h_s(t) l_c + \frac{1}{\mu_0} b_0(t) l_g, \tag{61}$$

where h_s is the magnetic field strength on the surface of the core lamination, l_c is the magnetic path length, l_g the air gap length and μ_0 the permeability of free space.

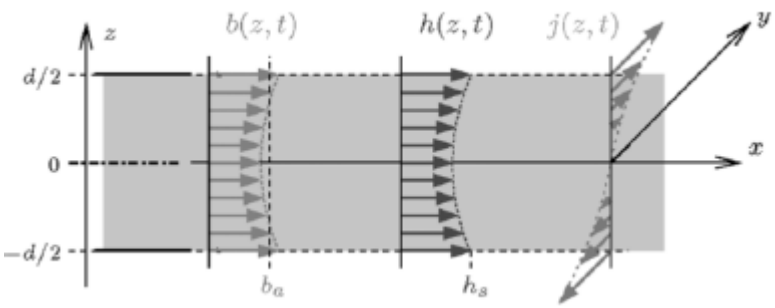

Figure 28: *Variation of h, b, and j through lamination of thickness d* [47]

The eddy current losses are calculated by solving the 1-d eddy current diffusion equation. Figure 28 shows a lamination of thickness d in the z-direction. The conductivity σ of the lamination is assumed to be constant and carries flux density $b(z,t)$ along the x-axis. The magnetic field strength $h(z,t)$ is linked to $b(z,t)$ by the constitutive law [47]

$$h = h_{\mathrm{hy}}\big(b(t)\big) + c_{\mathrm{ex}} \left|\frac{db(t)}{dt}\right|^{-0.5} \frac{db(t)}{dt}, \tag{62}$$

where c_{ex} is the excess loss coefficient which is determined from loss data found in the manufacturer data sheet for the material M330-35A. The magnetic field in the lamination is governed by the 1-d diffusion equation

$$\frac{\partial^2 h(z,t)}{\partial z^2} = \sigma \frac{\partial b(z,t)}{\partial t}. \tag{63}$$

The diffusion equation describes how the distribution of flux in the lamination changes over time. Assuming that the skin effect is negligible and that the flux density is uniform throughout the cross-section of the lamination, integrating (63) twice and requiring (62) to be satisfied on average, a low frequency approximation of the surface field strength in the laminations is obtained from

$$h_{\mathrm{s}}(t) = h_{\mathrm{hy}}\big(b_0(t)\big) + \frac{\sigma d^2}{12}\frac{db_0(t)}{dt} + c_{\mathrm{ex}}\left|\frac{db_0(t)}{dt}\right|^{-0.5}\frac{db_0(t)}{dt}, \tag{64}$$

which can be taken as three separate parts. The first term represented by the function h_{hy} is the static hysteresis curve. The static hysteresis curve is the core's history-dependent and frequency independent magnetisation curve. The second term represents the eddy current losses and the third term the excess losses.

The instantaneous power densities for the rate-of-change of the magnetic field energy (p_{hy}), eddy current losses (p_{cl}), and excess losses (p_{ex}) are found from

$$p_{\mathrm{hy}}(t) = h_{\mathrm{hy}}\big(b_0(t)\big)\frac{db_0(t)}{dt}, \tag{65}$$

$$p_{\mathrm{cl}}(t) = \frac{\sigma d^2}{12}\left(\frac{db_0(t)}{dt}\right)^2, \tag{66}$$

$$p_{\mathrm{ex}}(t) = c_{\mathrm{ex}}\left|\frac{db_0(t)}{dt}\right|^{1.5}. \tag{67}$$

The total core losses can then be found from the sum of multiplying (65)-(67) by the volume of the core

$$V_{\mathrm{Fe}} = A_{\mathrm{Fe}} l_{\mathrm{Fe}}, \tag{68}$$

and averaging over one period of the fundamental frequency. The DC winding losses are found simply from averaging $Ri^2(t)$ over the same period. The AC winding losses are neglected.

4. DESIGN AND SIMULATION RESULTS

This chapter presents the results of the design process based on the area-product method for toroidal filter inductors and also the results gained from modelling of the generated designs using the Simulink inductor model.

4.1 Filter inductor design results

Since the inductors selected to be prototyped are wound by hand without a winding shuttle, the value of k_{u} = 0.4 is suitable and the recommended 0.15-0.25 for toroids is disregarded resulting in smaller required core sizes. 2.12 mm diameter winding wire is used in the construction of the prototypes so the value of 1.42 A/mm^2 is used for the current density J_{m}. The maximum value typically used in designs is 5 A/mm^2. Filter inductors were designed for an inverter with a 300 V DC input voltage, with a switching frequency of 20 kHz feeding a 10.4 Ω resistive load requiring an output current of 5 A with a maximum peak-to-peak ripple of 5 %. Using (13) a value of 10.6 mH is obtained for the filter inductors. The area-product for the core required using B_{m} = 1 T, I_{m} = 5 A, J_{m} = 1.42 A/mm^2, L_{ref} = 10.6 mH and k_{u} = 0.4 is 66.17 cm^4. 12 different possible core heights were selected between 12 mm and 80 mm. For each value of h, k_{d} was varied between 1.4 and 2.6 for 25 different values resulting in 300 different core geometries for the calculated area-product. Some important parameters output by the program are shown in Figure 29.

```
inductor design #:                1
area product:                     66.1664 cm^4
core cross-setional area:         169.3 mm^2
winding window area:              3908.24 mm^2
inductance:                       10.6 mH
core height:                      12 mm
kd:                               1.4
inner diameter:                   70.5416 mm
outer diameter:                   98.7583 mm
air gap length:                   19.5672 mm
number of turns:                  443
number of winding layers:         6
length of winding:                29.5274 m
length of winding turn:           66.6533 mm
winding resistance:               0.140484 ohms
weight of core:                   0.344425 kg
weight of winding:                0.927944 kg
total weight:                     1.27237 kg
```

Figure 29: *Inductor design program output example*

Once the designs have been created by the MATLAB script, some initial analysis can be made about their properties such as weights, air gap lengths, and geometries. For every 25 designs made, the core height increases for the next 25 designs made. Table 2 shows which core heights apply to which design numbers.

Table 2: *Core heights for specific design numbers*

Design number	Core height (mm)
1-25	12
26-50	13
51-75	15
76-100	20
101-125	25
126-150	30
151-175	35
176-200	40
201-225	50
226-250	60
251-275	70
276-300	80

Figure 30 shows the total weight of each design, comprised of the core weight and the winding weight. If the specific application of the inductor requires low weight, then inductors above a certain weight threshold can be disregarded and further analysis can be carried out on the remaining inductors depending on the requirements. For each core height, increasing the value of k_d – the ratio between the outer and inner diameter of the toroid – initially reduces the weight of the design before eventually increasing it. The heaviest cores have high values for k_d and have the highest core heights, with the lightest designs having core heights of 20 mm and 25 mm and low values of k_d.

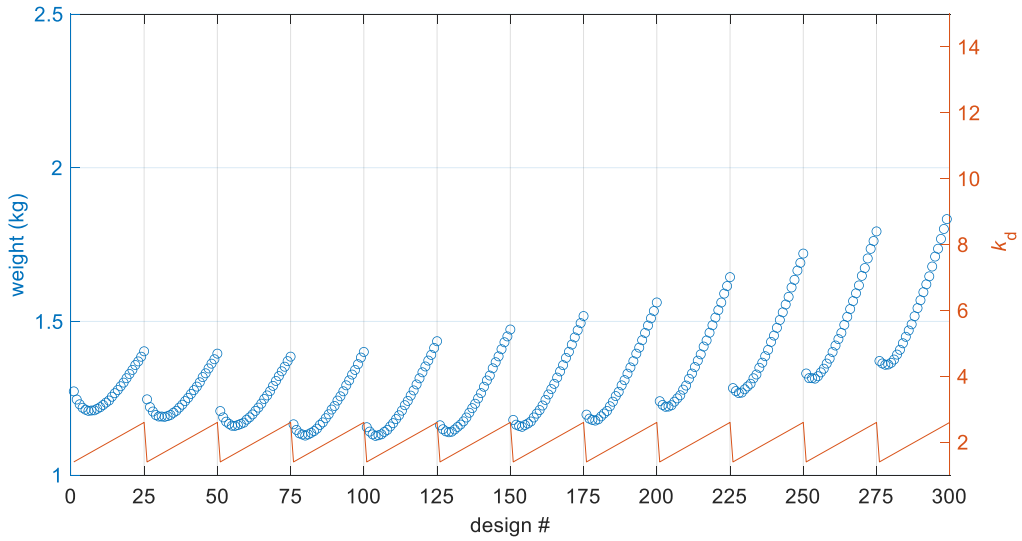

Figure 30: *Total weight of specific designs*

Figure 31 shows the air gap lengths of specific designs. Designs with lower core cross-sectional areas have the largest air gaps, with the air gap length reducing as k_d increases. Designs with longer air gap lengths can have higher winding losses due to fringing effects [48] .

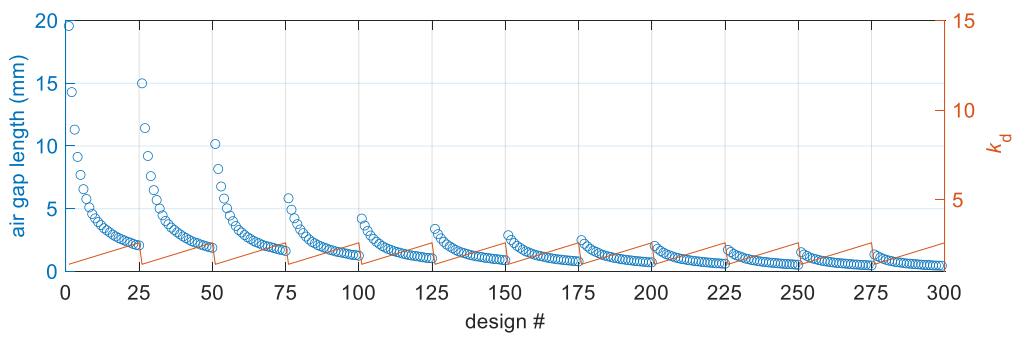

Figure 31: *Air gap lengths of specific designs*

Figure 32 shows the heights and outer diameters of the designed inductor cores. Taller inductors have smaller outer diameters and shorter inductors have larger outer diameters. In applications where height or width of the finished inductor is of concern, it is easy to analyse which of the designed inductors may or may not be suitable.

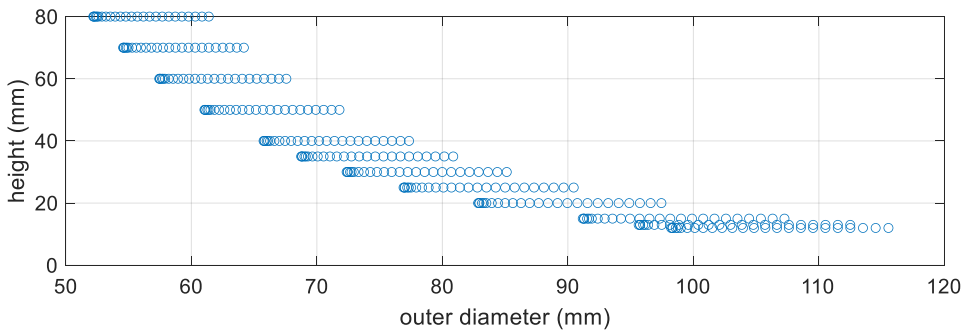

Figure 32: *Height versus outer diameter for inductor cores*

From the design program, inductors can be selected to be produced based on their weights and geometries and even cost. The other important factor is how efficient the inductors are and what kind of losses they produce. To obtain information about core and winding losses in the inductor, accurate simulation tools are needed which can compute losses based on information about the core geometry, windings, and material properties. Such a simulation tool is described in the next section.

4.2 Filter inductor simulation results

The parameters of each of the designed inductors were input into the MATLAB Simulink inductor model and a simulation was run on each inductor for two cycles of the fundamental frequency of 60 Hz. Table 3 shows the inductor parameters taken into account by the inductor simulation model. Table 4 shows the initial simulation parameters. Figure 33 shows the waveforms that can be viewed in the once the simulation has run.

Table 3: *Inputs to the simulation model*

Inductor parameter	Symbol
Number of turns	N
Core cross-sectional area	A_c
Magnetic path length	l_c
Fringing factor	F_f
Air gap length	l_g
Winding resistance	R
Air gap inductance	L_δ

Table 4: *Initial simulation parameters*

Simulation parameter	Initial value
Inverter input voltage (V_{DC})	300 V
Amplitude modulation ratio (m_a)	0.265
Switching frequency (f_{sw})	20 kHz
Output frequency (f)	60 Hz
Load resistance (R_L)	10.4 Ω

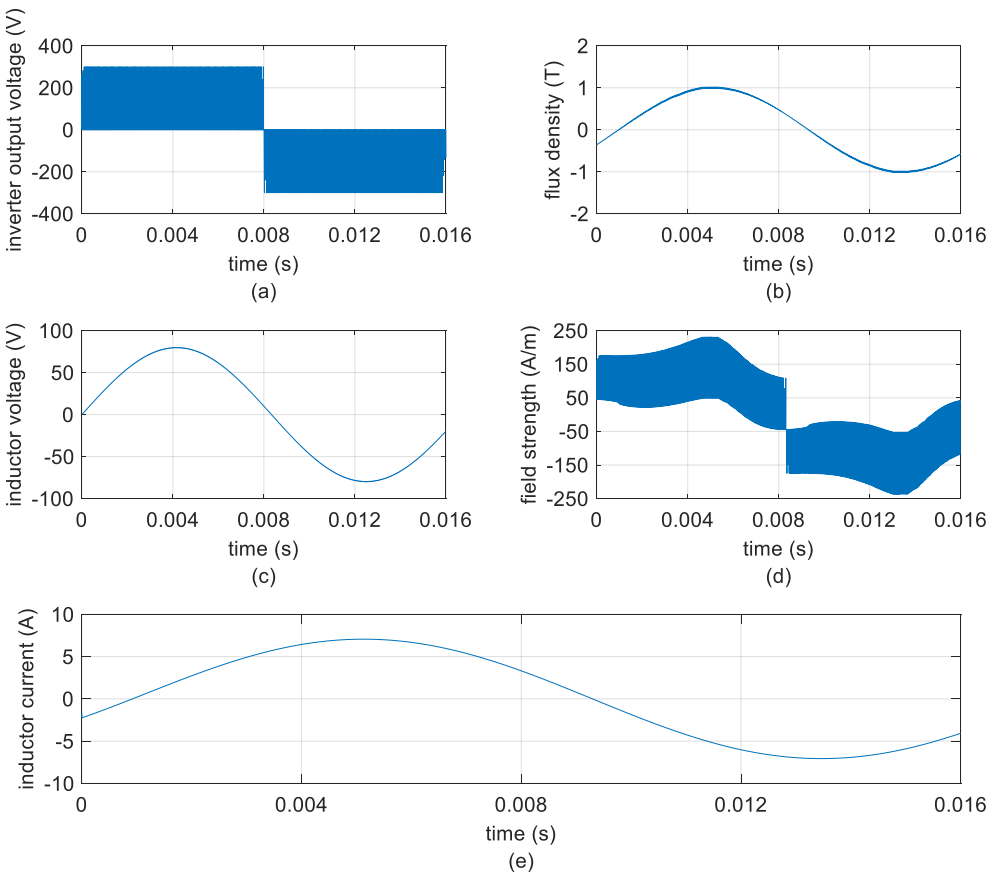

Figure 33: *Simulink model output signals: (a) Inverter output voltage, (b) Flux density, (c) Inductor voltage, (d) Field strength, (e) Inductor current*

Upon completion of the simulation of each inductor, plots were produced to analyse the losses in the inductors and how these were related to the variables k_{d} and h. Figure 34 shows total, core and winding losses for each of the designed inductors. It can be seen that cores with large cross-sectional areas have the highest total losses. The total losses are dominated by the core losses which are high for inductors with large cross-sectional areas. The inductors with the highest core losses have the lowest winding losses.

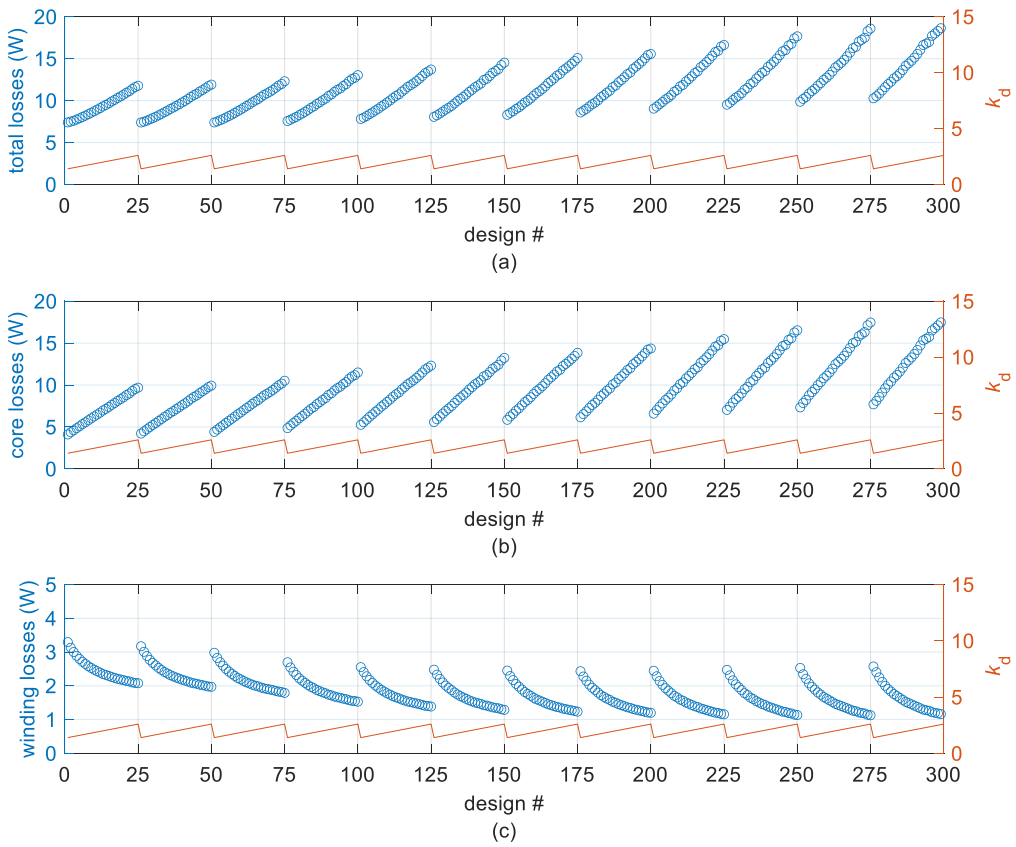

Figure 34: *Losses in designed inductors, (a) Total losses, (b) Core losses, (c) Winding losses*

Since the simulation model calculates each separate component of the core losses, these losses can be separately analysed. Figure 35 shows each component of the core losses for each inductor. It can be seen that each component of the losses increases as the cross-sectional area of the inductor core increases. The core losses are dominated by the eddy current losses which contribute the most to the core losses followed by the excess losses. The hysteresis losses are the smallest component of the core losses.

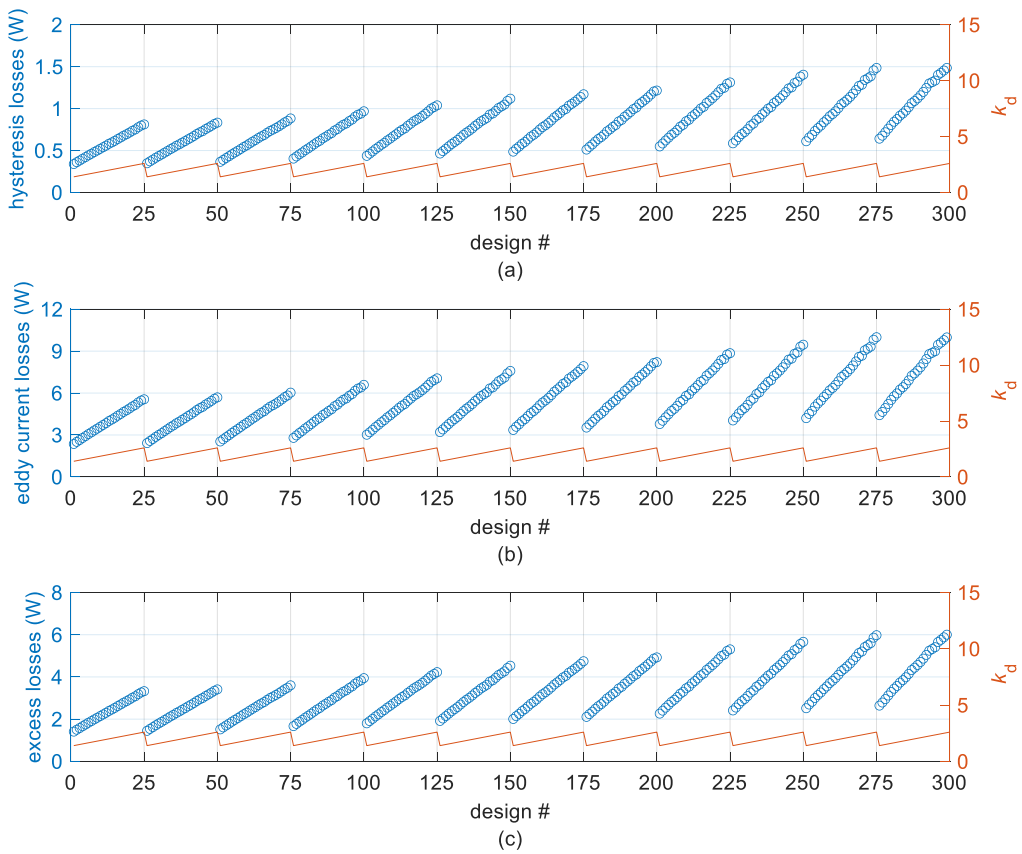

Figure 35: *Breakdown of core losses for designed inductors. (a) Hysteresis losses, (b) Eddy current losses, (c) Excess losses*

Some analysis can be carried out into how losses are linked to the weight and geometry of the inductors and what kind of trade-offs may have to be made in selecting inductors for different purposes. Figure 36 shows how core losses and winding losses vary with the weight of the inductors. It can be seen that there is a point where designs have low losses and low weight. Attempts to reduce losses from this point onwards leads to an increase in weight.

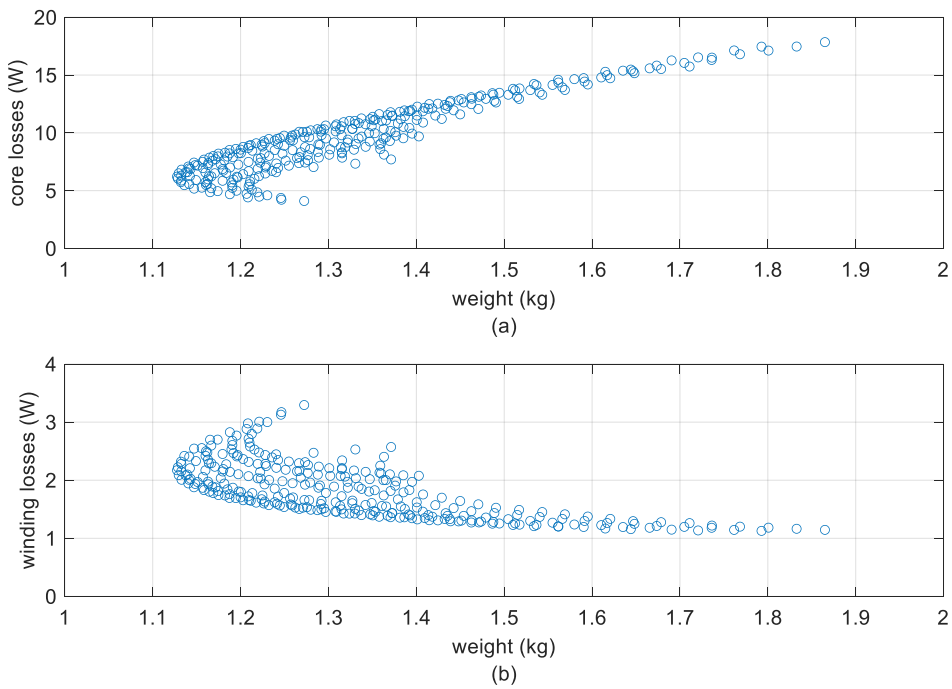

Figure 36: *(a) Core losses versus inductor weight, (b) Winding losses versus inductor weight*

In Figure 37 the effect of the air gap length on losses can be examined. Increasing the air gap length reduces the core losses but tends to increase the winding losses. The number of turns of the winding increases when the air gap length increases leading to higher winding resistance. Since the total losses are dominated by the core losses, the effect of the air gap length on the core losses may be of the most interest.

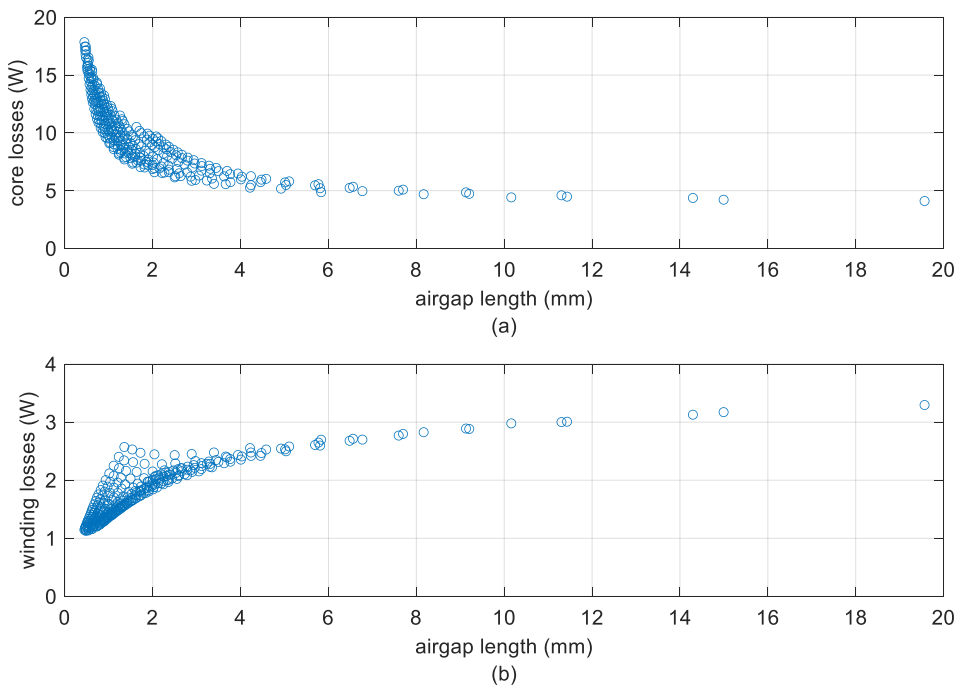

Figure 37: *(a) Core losses versus air gap length, (b) Winding losses versus air gap length*

When designing inductors, one important factor, along with size and loss concerns, is cost. As an example, and using a simple 2 to 1 ratio of winding material cost and core material cost as in [49], it can be seen from Figure 38 how the design method can be used to find inductors with suitable price and performance. The winding material cost is set to 10 €/kg and the core material cost is set to 5 €/kg as also in [44]. More accurate prices based on the true cost of materials can easily be entered. From Figure 38 it can be seen that in the example case, there is a point where weight and the price are low. Reducing the weight further leads to price increases. The situation is similar for the total losses. In this way, it is possible to use the data gained from the design program and simulations to find optimal designs for a specific application.

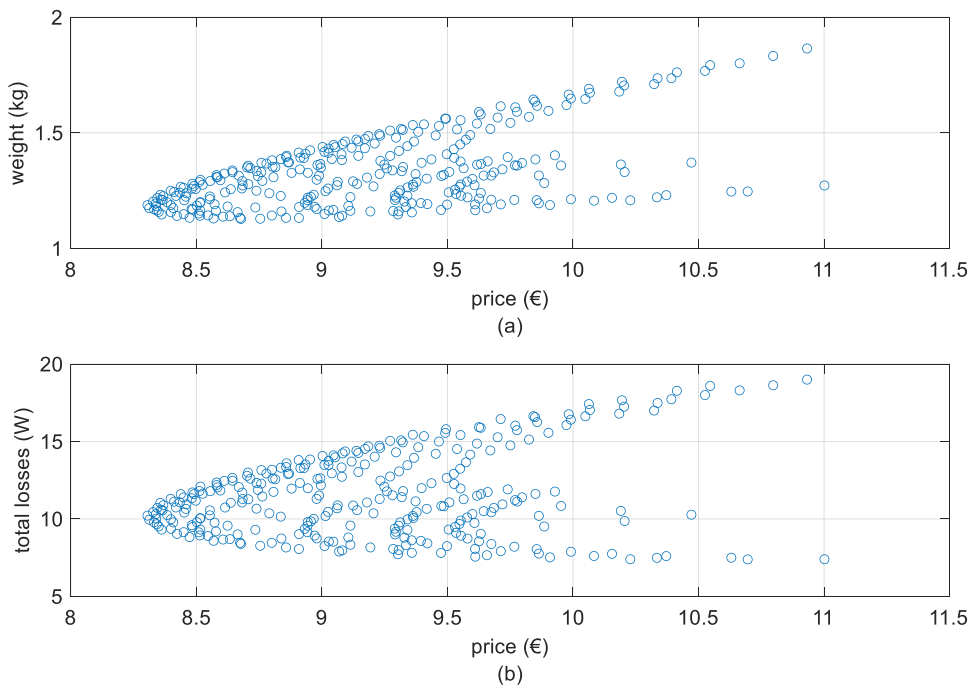

Figure 38: *Example of cost analysis. (a) Weight versus price, (b) Total losses versus price*

5. EXPERIMENTAL VALIDATION

After simulating the behaviour of each of the designed inductors using the MATLAB Simulink inductor model, some of the designs were selected to be constructed to validate the design process and inductor model. This chapter discusses the selected cores, the construction methods, construction process, and measurement process.

5.1 Selected cores

Of interest to construct were the inductors with the highest and lowest total losses, the highest and lowest total weight, and the longest and shortest air gap lengths. Since some inductors possessed one or more of these qualities, three inductors were selected to be constructed. Table 5 shows the selected inductors and their specifications.

Table 5: *Specifications of selected inductors*

Inductor parameter	Design 1	Design 104	Design 300
Area-product (cm^4)	66.17	66.17	66.17
Core cross-sectional area (mm^2)	169.3	341.48	1511.13
Winding window area (mm^2)	3908.24	1937.64	437.86
Height (mm)	12	25	80
k_d	1.4	1.55	2.6
Outer diameter (mm)	98.76	76.99	61.39
Inner diameter (mm)	70.54	49.67	23.61
Air gap length (mm)	19.57	2.86	0.44
Number of winding turns	443	219	50
Number of winding layers	6	4	2
Winding resistance (Ω)	0.14	0.09	0.05
Core weight (kg)	0.34	0.52	1.54
Winding weight (kg)	0.93	0.61	0.32
Total weight (kg)	1.27	1.12	1.86

Figure 39 shows technical drawings of Design 1 and Design 300. It is easy to see how different the geometries can be for cores with the same area-product.

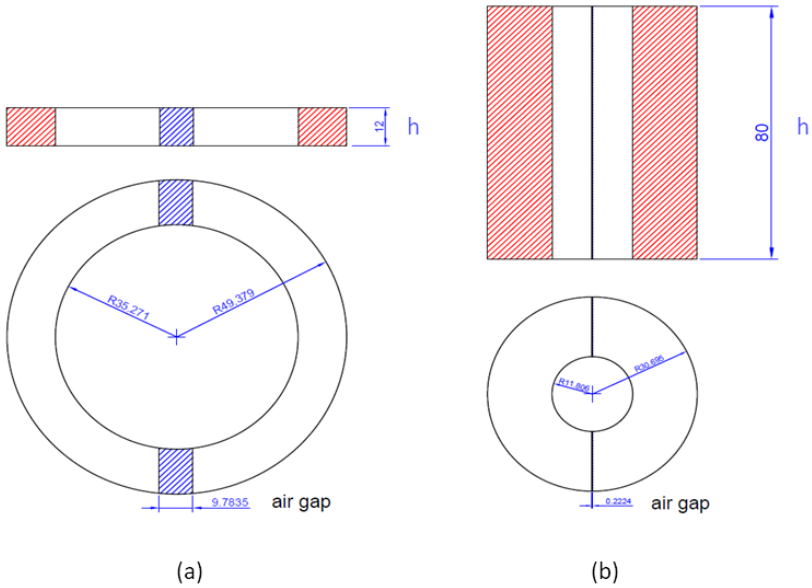

Figure 39: *(a) Dimensions of Design 1, (b) Dimensions of Design 300*

5.2 Construction process

The prototype cores were made by welding together stacks of laminations cut to the dimensions created by the design program. Welding is a common technique used in the manufacturing of cores to join the laminations together [50]. Welding essentially fuses the laminations together through heating until melting point. The laminations were cut into shape by a laser cutting machine. The first step in creating the cores was to create a template of the dimensions of the laminations to be laser cut as shown in Figure 40 (a). Then, from the rectangular sheets of M330-35A non-grain-oriented silicon steel shown in Figure 40 (b), each laminated piece is laser cut into shape as shown in Figure 40 (c). The laser cut laminations are then stacked together using as many laminations as needed to reach the desired core height as shown in Figure 40 (d). A core stacking factor of 0.95 is used to account for space taken up by the insulating coating on the laminations. Finally, to secure the laminations together, three welding seams are created on each core half. Figure 40 (e) shows the three welded inductor cores ready to have spacers inserted to create air gaps. From left to right in Figure 40 (e) are Designs 1, 104, and 300.

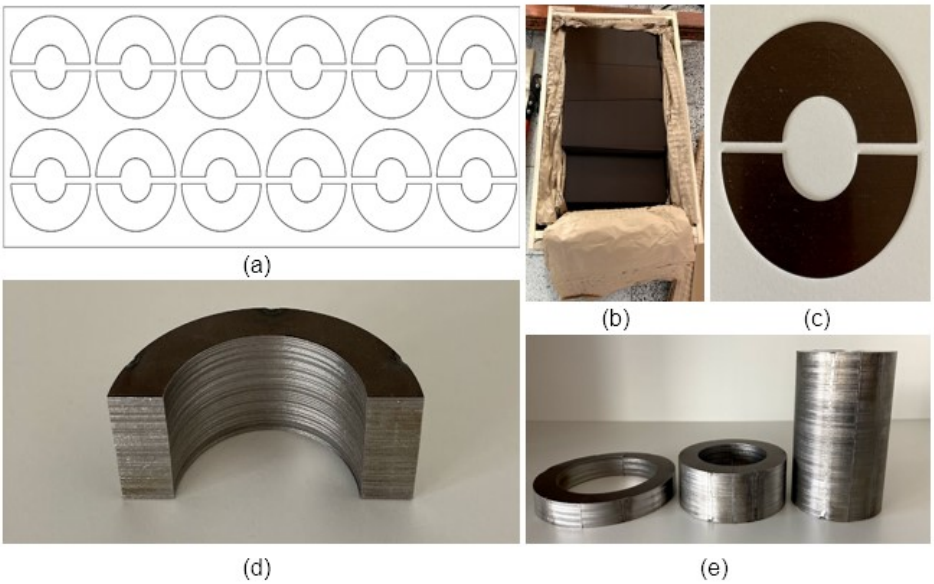

Figure 40: *(a) Inductor lamination template, (b) Sheets of M330-35A silicon steel, (c) Individual laminations cut to shape, (d) Stacked laminations, (e) Welded inductor cores*

Once the laminations have been stacked and joined together, spacers are inserted to create air gaps. The total air gap length is distributed over two air gaps of half the length. Since Designs 104 and 300 have short air gaps, the spacers are created by layering together very thin sheets of Kapton tape. For the large air gap length of design 1, the spacers are created by 3-d printing plastic pieces. Figure 41 (a) shows the Kapton tape spacer, and Figure 41 (b) shows the 3-d printed plastic spacer. A thin layer of glue is used to join together the core halves with the spacers to create the finished inductor core.

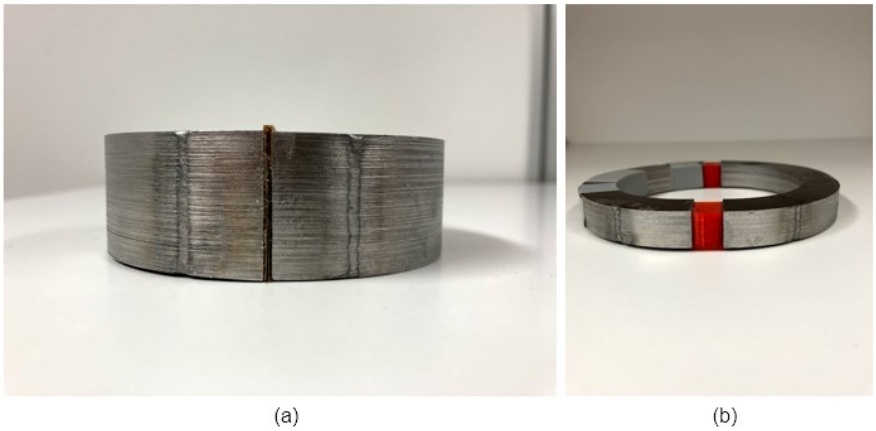

Figure 41: *(a) Air gap spacer made from layered Kapton tape, (b) Air gap spacer made from 3-d printed plastic*

After constructing the cores, the winding of the inductor is wound over the core by hand using insulated copper wire. The winding turns are distributed over the core adhering to the number of layers calculated by the design program. Figure 42 shows a completed inductor with core and windings.

Figure 42: *Completed inductor with core and windings*

5.3 Measurement results

For each of the three constructed cores, measurements of inductance were taken to assess how well the constructed cores met the desired values for inductance and to compare the results with the Simulink simulation model. Inductor Design 104 was also constructed again using different construction techniques. The laminations of the core were glued together – a technique known as sticking – instead of welded, and the individual laminations were cut using electric discharge machining (EDM) instead of laser cutting to compare how the different construction techniques affected the inductance values of the completed inductors. For all inductors the measurements were taken using the GW Instek LCR-8101G LCR (inductance (L), capacitance (C), resistance (R)) meter using 1 V AC over a frequency range of 20-200Hz.

Figure 43 shows the measurement results for the three inductor designs that were chosen to be constructed. The required inductance value was 10.6 mH at 60 Hz and the cores were constructed by welding together laminations which had been laser cut. It can be seen from Figure 43 that the constructed inductors do not meet the required inductance value, with some performing better than others. Design 1 has the closest inductance value to the required value at 8.21 mH at 60 Hz. Both Design 1 and Design 300 have relatively steady inductance values as frequency increases above 60 Hz. The inductance value of Design 104 decreases across the full range of frequencies measured. Since the Simulink model verified the inductance values of the designed inductors and the Simulink model itself was verified in [46] through comparison with measurements, if the fringing factor used in the design and simulation process is assumed to be accurate, it may be concluded that the discrepancy between designed values and measured values of inductance can be mainly attributed to shortcomings in the construction process.

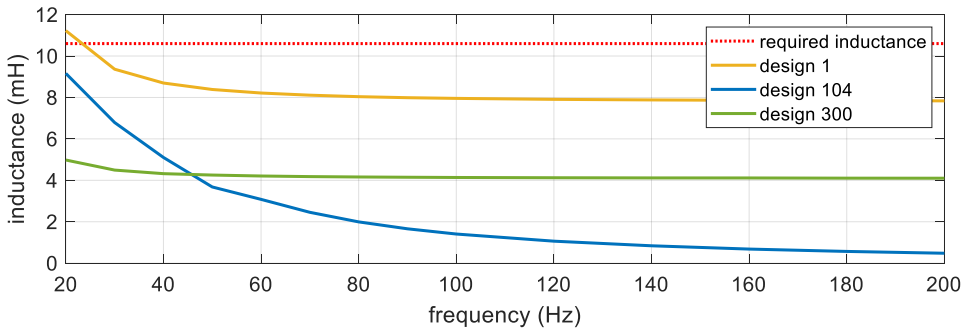

Figure 43: *Measured inductance value for inductors constructed using welded laser cut laminations*

With reference to the measured values of inductance shown in Figure 43, it should be noted that the best performing inductor had the longest air gap. Rearranging (53) shows that for inductors with very small air gaps, any discrepancy between the calculated air gap length value and the air gap length value in the constructed inductor can have a big impact on the inductance value of the constructed inductor. Table 6 shows the impact a 0.25 mm discrepancy in the air gap length can have on the inductance value of constructed inductors.

Table 6: *Effect of air gap length on inductance*

	Air gap length (l_g)	**Inductance value at $l_g - 0.25$ mm**	**Inductance at value at l_g**	**Inductance value at $l_g + 0.25$ mm**
Design 1	19.57 mm	10.73 mH	10.60 mH	10.47 mH
Design 104	2.86 mm	11.60 mH	10.60 mH	9.76 mH
Design 300	0.44 mm	22.88 mH	10.60 mH	6.83 mH

From Table 6 it can be seen how small changes in the air gap length can have a great impact on the inductance value. Although every care is taken in the construction process to produce spacers to the exact specification of the design values, differences of 0.25 mm are possible. Glue between the spacers and the core can add to the air gap length and compression of the spacer when core halves are pushed together can reduce the air gap length. For designs with larger air gaps the effect of small discrepancies is less pronounced which may explain the better performance of Design 1. The designed inductors have the air gap length distributed over two air gaps. It is possible to easily modify the design program to distribute the air gap across only one gap. This way the need for the production of spacers is eliminated, however, the air gap length could still be influenced by the tolerances of the cutting method of the laminations and since the purpose of distributed air gaps is to reduce the effect of the fringing flux, related losses would be increased [51].

Measurements were also carried out for Design 104 with a different construction method. This time, instead of welding the laminations together, they are joined together using thin layers of glue. The laminations were also created through EDM cutting instead of laser cutting. Figure 44 shows the measured inductance values for Design 104 for the welded core and the glued core. It can be seen that the glued core performs much better than the welded core, having an inductance value of 8.03 mH compared to 3.08 mH for the welded core. Although both the cutting and joining methods of the laminations were changed, the large frequency-dependency of the inductance in the welded cores indicates that welding is the dominant deteriorating aspect of the construction process due to eddy currents flowing through the welding seam.

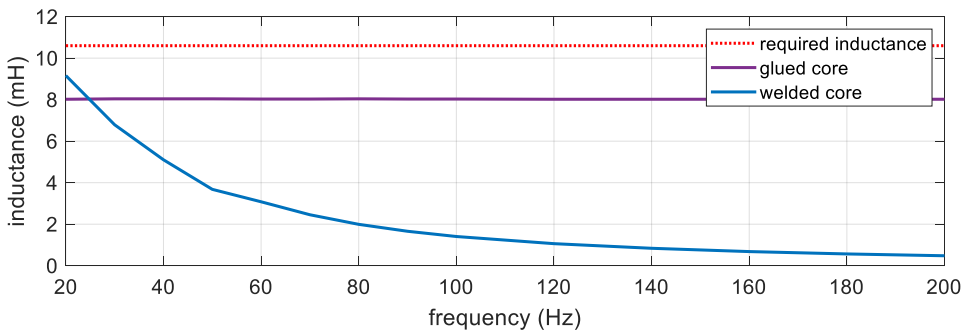

Figure 44: *Inductance values for Design 104 for different construction methods*

Laminations must be joined together to provide a mechanically strong core that can withstand the forces it is subjected to without deforming. The laminations must also remain stationary in relation to each other since movement can cause wear of the insulating coating leading to an increase in eddy current losses [52]. Welding the laminations together can provide mechanical strength but at the expense of a degradation of the magnetic properties of the core material, especially in the area of the weld zone. The welding process also damages the insulating material of the laminations causing short circuits between the laminations which increase eddy current losses. The degradation in the magnetic properties of the core is more pronounced when the area of the welding zone is large in relation to the area of the lamination. The cores produced by welding laminations together each had six welding passes each, three on each half of the core. [53] found that reducing the number of welding passes reduced the effect on the magnetic properties of core materials. One solution could, therefore, be to reduce the number of welding passes on the designs to four providing mechanical strength is still sufficient enough. It was also found in [53] that sticking had negligible effects on the magnetic properties of core materials.

To create the semi-circular laminations which make up the toroidal core of the inductor, shapes must be cut out of laminated sheets. The cutting process can have a negative effect on the magnetic properties of the lamination material. In the welded cores, the laminations are cut into shape by laser cutting. The laser cutting process subjects the laminations to thermal stress which can change the magnetic properties of the material. When cut by mechanical means, the changes in the magnetic properties of the material are localised around the cutting edge. For laser cutting it was found that the magnetic properties of whole laminations were affected for laminations with widths of up to 15 mm [54]. In a study of the same M330-35A material as used in the construction of the inductor cores, EDM cutting was found to have the lowest impact upon the magnetic properties of the material when compared to mechanical cutting or laser cutting, with

laser cutting having the largest effect [55]. It was also found that for cores with geometries smaller than 30 mm such as in the three constructed designs which have lamination widths between 13.66-18.99 mm, the magnetic properties of the material vary significantly compared to the manufacturers data sheet, especially when cut by laser. [56] found decreases in permeability of up to 35 % in laminations cut by laser at 1.5 T and 50 Hz and decreasing further as the flux density decreases. The effects of the laser cutting on the laminations may be reversed somewhat through annealing but this adds to the costs of the manufacturing process. The EDM cutting process is much slower than laser cutting but for the purposes of creating prototype cores, may be less deleterious to the magnetic properties.

Changing the construction method from welding and laser cutting to sticking and EDM cutting vastly improved the inductance value of the constructed inductors so this would be a recommended process in future construction. The remaining discrepancy in inductance value for Design 104 may be due to the air gap spacing. Around a 0.86 mm increase in the air gap length for Design 104 could account for the difference between the measured inductance and calculated inductance and is in the possible error range for the construction methods used. Similarly, for Design 1 which had a large air gap, the difference between the measured value and the calculated value could be explained by the effect of the welding and laser cutting processes. It is possible that Design 300, with the smallest air gap length, suffered from both the effects of welding and laser cutting as well as the effect of discrepancies in the air gap length. Of the inductors constructed the two best performing achieved 75-77 % of the required inductance value. A professionally built toroidal inductor with two air gaps purchased during this thesis work was found to achieve 87.4 % of the required inductance value so it is evident that there are challenges in producing these kinds of inductors.

6. CONCLUSIONS

It was the goal of this thesis to find a method of quickly designing and producing toroidal filter inductors. The design process that was developed was able to quickly produce multiple possible designs, where weight, geometry, and cost could quickly be determined and used to inform selection choice. It was also a goal to further develop the Simulink inductor simulation model by comparing the simulation results to measurement results. The simulation tool was able to provide information on the core and winding losses of the designed inductors to further inform selection. Ultimately, power losses in the constructed inductors were not measured since the constructed inductors did not meet the required inductance values.

Although a valid design method was developed for the design of toroidal filter inductors, challenges in the construction process were highlighted. It was found that the method used to cut and join the laminations had a large effect on the properties of the constructed inductors. For future construction efforts, sticking and EDM cutting of the laminations is recommended. Great care in achieving high accuracy is also needed when constructing cores with very small air gaps.

The inductors were designed by varying geometric parameters, but the design program can be easily adapted to adjust any parameter of interest. In future it may be of use to incorporate design factors into the design process which can account for the changes in material properties that occur in the manufacturing process. The inductor simulation model makes use of material specific data from manufacturer catalogues but can also easily make use of data obtained from measurements of magnetic properties after manufacturing processes have taken place to provide manufacturing process specific analysis of losses. Both the design tool and inductor simulation model can be useful in the development of efficient and cost-effective filter inductors for DC/AC inverters.

REFERENCES

[1] G. Zhang, Z. Li, B. Zhang, and W. A. Halang, “Power electronics converters: Past, present and future,” *Renewable and Sustainable Energy Reviews*, vol. 81. Elsevier Ltd, pp. 2028–2044, Jan. 01, 2018. doi: 10.1016/j.rser.2017.05.290.

[2] J. D. van Wyk and F. C. Lee, “On a future for power electronics,” *IEEE J Emerg Sel Top Power Electron*, vol. 1, no. 2, pp. 59–72, Jun. 2013, doi: 10.1109/JESTPE.2013.2271499.

[3] J. W. Kolar, D. Bortis, and D. Neumayr, “The ideal switch is not enough,” in *Proceedings of the International Symposium on Power Semiconductor Devices and ICs*, Jul. 2016, vol. 2016-July, pp. 15–22. doi: 10.1109/ISPSD.2016.7520767.

[4] P. A. Kyaw, A. L. F. Stein, and C. R. Sullivan, “Fundamental Examination of Multiple Potential Passive Component Technologies for Future Power Electronics,” *IEEE Trans Power Electron*, vol. 33, no. 12, pp. 10708–10722, Dec. 2018, doi: 10.1109/TPEL.2017.2776609.

[5] I. Robertson. Sinclair, “Chapter 1 - Fundamentals,” in *Passive components for circuit design*, 1st edition., Oxford: Newnes, 2000.

[6] M. März, A. Schletz, B. Eckardt, S. Egelkraut, and H. Rauh, “Power electronics system integration for electric and hybrid vehicles,” in *2010 6th International Conference on Integrated Power Electronics Systems*, 2010, pp. 1–10.

[7] A. Walker, G. Vakil, and C. Gerada, “Novel Core Designs to Miniaturise Passive Magnetic Components,” in *2018 IEEE Transportation and Electrification Conference and Expo, ITEC 2018*, Aug. 2018, pp. 135–139. doi: 10.1109/ITEC.2018.8449959.

[8] K. B. Park, F. Kieferndorf, U. Drofenik, S. Pettersson, and F. Canales, “Weight minimization of LCL filters for high power converters,” in *9th International Conference on Power Electronics - ECCE Asia: “Green World with Power Electronics”, ICPE 2015-ECCE Asia*, Jul. 2015, pp. 142–149. doi: 10.1109/ICPE.2015.7167778.

[9] D. Shuai and Z. Qianfan, “Analysis and Control of Current Ripples of Z-Source Inverters,” *IEEE Access*, vol. 8, pp. 41220–41228, 2020, doi: 10.1109/ACCESS.2020.2976811.

[10] C. T. Pan, C. M. Lai, and Y. L. Juan, “Output current ripple-free PWM inverters,” *IEEE Transactions on Circuits and Systems II: Express Briefs*, vol. 57, no. 10, pp. 823–827, 2010, doi: 10.1109/TCSII.2010.2058596.

[11] M. J. Schutten, R. L. Steigerwald, and J. A. Sabaté, “Ripple current cancellation circuit,” in *Conference Proceedings - IEEE Applied Power Electronics Conference and Exposition - APEC*, 2003, vol. 1, pp. 464–470. doi: 10.1109/apec.2003.1179254.

[12] A. A. Khan *et al.*, “Coupled-inductor buck-boost inverter with reduced current ripple,” *IEEE Trans Power Electron*, vol. 35, no. 8, pp. 7933–7946, Aug. 2020, doi: 10.1109/TPEL.2019.2962668.

[13] W. J. Gu and R. Liu, “Study of volume and weight vs. frequency for high-frequency transformers,” in *PESC Record - IEEE Annual Power Electronics Specialists Conference*, 1993, pp. 1123–1129. doi: 10.1109/pesc.1993.472059.

[14] W. G. Hurley and W. H. Wölfe, *Transformers and Inductors for Power Electronics Theory, Design and Applications*. Chichester: John Wiley & Sons, 2013.

[15] J. Wang, X. Yuan, T. Riipinen, J. Pippuri-Makelainen, S. Metsa-Kortelainen, and T. Lindroos, “Evaluation of 3D Printed Cobalt Iron Cores for Filter Inductors,” *IEEE Trans Magn*, vol. 56, no. 8, Aug. 2020, doi: 10.1109/TMAG.2020.3000417.

[16] F. Forest, E. Labouré, T. Meynard, and M. Arab, “Analytic design method based on homothetic shape of magnetic cores for high-frequency transformers,” *IEEE Trans Power Electron*, vol. 22, no. 5, pp. 2070–2080, Sep. 2007, doi: 10.1109/TPEL.2007.904251.

[17] S. Kim, “Chapter 7 - Pulse width modulation inverters,” in *Electric Motor Control*, Elsevier, 2017, pp. 265–340. doi: https://doi.org/10.1016/B978-0-12-812138-2.00007-6.

[18] D. W. Hart, “Chapter 8 - Inverters,” in *Power electronics*, New York: McGraw-Hill, 2011, pp. 331–386.

[19] M. Arab, A. Zegaoui, P. Petit, A. Djahbar, and M. Aillerie, “Output-voltage feedback control topology for inverters dedicated to renewable energy systems,” *International Journal of Circuit Theory and Applications*, vol. 45, no. 12, pp. 2270–2280, Dec. 2017, doi: 10.1002/cta.2349.

[20] S. K. Mandal, “Chapter 11 - Inverters,” in *Power Electronics*, New Delhi: McGraw Hill Education (India), 2014, pp. 679–789.

[21] F. C. de La Rosa, *Harmonics and power systems*, Second edition. Boca Raton: CRC/Taylor & Francis, 2006.

[22] “Electric motor control applications: The use of square waves to operate motors,” *Industrial Electronics*, 2022. https://www.industrial-electronics.com/emct_2e_6i.html (accessed Oct. 25, 2022).

[23] M. Asker and H. Kiliç, “Modulation Index and Switching Frequency Effect on Symmetric Regular Sampled SPWM,” *European Journal of Technic*, vol. 7, pp. 102–109, Nov. 2017, doi: 10.23884/ejt.2017.7.2.04.

[24] Ned. Mohan, T. M. Undeland, and W. P. Robbins, *Power electronics: converters, applications, and design*. John Wiley & Sons, 2003.

[25] L. G. Franquelo, J. Rodriguez, J. I. Leon, S. Kouro, R. Portillo, and M. A. M. Prats, “The age of multilevel converters arrives,” *IEEE Industrial Electronics Magazine*, vol. 2, no. 2, pp. 28–39, Jun. 2008, doi: 10.1109/MIE.2008.923519.

[26] H. Cha and T. K. Vu, “Comparative analysis of low-pass output filter for single-phase grid-connected photovoltaic inverter,” in *Conference Proceedings - IEEE Applied Power Electronics Conference and Exposition - APEC*, 2010, pp. 1659–1665. doi: 10.1109/APEC.2010.5433454.

[27] P. Channegowda and V. John, “Filter Optimization for Grid Interactive Voltage Source Inverters,” *IEEE Transactions on Industrial Electronics*, vol. 57, no. 12, pp. 4106–4114, 2010, doi: 10.1109/TIE.2010.2042421.

[28] J. M. Sosa, P. R. Martinez-Rodriguez, G. Escobar, G. Vazquez, and A. A. Valdez-Fernandez, “Active Power Injection Control for Power Converters Connected to the Grid Through an L Filter,” *Electric Power Components and Systems*, vol. 45, no. 6, pp. 660–671, Apr. 2017, doi: 10.1080/15325008.2017.1291768.

[29] H. Yamaji, T. Shimizu, K. Takano, and H. Ishii, “Iron loss evaluation of AC filter inductor core in a PWM inverter; Iron loss evaluation of AC filter inductor core in a PWM inverter,” 2009.

[30] D. Shuai and Z. Qianfan, “Analysis and Control of Current Ripples of Z-Source Inverters,” *IEEE Access*, vol. 8, pp. 41220–41228, 2020, doi: 10.1109/ACCESS.2020.2976811.

[31] A. van den. Bossche and Vencislav. Valchev, *Inductors and Transformers for Power Electronics*, 1st edition. Boca Raton: Taylor & Francis, 2005.

[32] M. K. Kazimierczuk, *High-Frequency Magnetic Components*. Wiley Publishing, 2009. doi: 10.5555/1822469.

[33] A. Hanif, “Measurement of Core Losses in Toroidal Inductors with Different Magnetic Materials,” Master’s thesis, Tampere University of Technology, Tampere, 2017.

[34] C. W. T. McLyman, *Transformer and inductor design handbook*. CRC Press, 2011.

[35] R. Clarke, “Magnetism: quantities, units and relationships,” 2014. http://info.ee.surrey.ac.uk/Workshop/advice/coils/terms.html (accessed Oct. 25, 2022).

[36] A. Oliveri, M. Lodi, and M. Storace, “Nonlinear models of power inductors: A survey,” *International Journal of Circuit Theory and Applications*, vol. 50, no. 1, pp. 2–34, Jan. 2022, doi: 10.1002/cta.3147.

[37] F. D. Tan, J. L. Vollin, and S. M. Cuk, “Practical approach for magnetic core-loss characterization,” *IEEE Trans Power Electron*, vol. 10, no. 2, pp. 124–130, Mar. 1995, doi: 10.1109/63.372597.

[38] N. Kondrath and M. K. Kazimierczuk, “Inductor winding loss owing to skin and proximity effects including harmonics in non-isolated pulse-width modulated dc-dc converters operating in continuous conduction mode,” *IET Power Electronics*, vol. 3, no. 6, pp. 989–1000, Nov. 2010, doi: 10.1049/iet-pel.2009.0299.

[39] M. Bartoli, A. Reatti, and M. K. Kazimierczuk, “Modelling iron-powder inductors at high frequencies,” in *Proceedings of 1994 IEEE Industry Applications Society Annual Meeting*, 1994, vol. 2, pp. 1225–1232 vol.2. doi: 10.1109/IAS.1994.377550.

[40] F. M. M. Rahman, “Converter-side inductor design for a grid-connected converter equipped with an LCL filter,” Master’s thesis, Aalto University, Espoo, 2016.

[41] D. C. Jiles and D. L. Atherton, “Theory of ferromagnetic hysteresis (invited),” *J Appl Phys*, vol. 55, no. 6, pp. 2115–2120, 1984, doi: 10.1063/1.333582.

[42] P. Beckley and G. K. Sujan, “Steels, Silicon Iron-Based: Magnetic Properties,” in *Encyclopedia of Materials: Science and Technology (Second Edition)*, Elsevier, 2016. doi: 10.1016/b978-0-12-803581-8.02475-9.

[43] R. C. Smith and C. L. Hom, “Domain Wall Theory for Ferroelectric Hysteresis,” *J Intell Mater Syst Struct*, vol. 10, no. 3, pp. 195–213, 1999, doi: 10.1177/1045389X9901000302.

[44] P. Hammond, “Chapter 7 - The magnetic effects of iron,” in *Electromagnetism for engineers: an introductory course*, Pergamon Press, 1986.

[45] M. K. Kazimierczuk and H. Sekiya, “Design of AC resonant inductors using area product method,” in *2009 IEEE Energy Conversion Congress and Exposition*, 2009, pp. 994–1001. doi: 10.1109/ECCE.2009.5316501.

[46] P. Rasilo, W. Martinez, K. Fujisaki, J. Kyyra, and A. Ruderman, “Simulink model for PWM-supplied laminated magnetic cores including hysteresis, eddy-current, and excess losses,” *IEEE Trans Power Electron*, vol. 34, no. 2, pp. 1683–1695, Feb. 2019, doi: 10.1109/TPEL.2018.2835661.

[47] J. Gyselinck, R. v. Sabariego, and P. Dular, “A nonlinear time-domain homogenization technique for laminated iron cores in three-dimensional finite-element models,” *IEEE Trans Magn*, vol. 42, no. 4, pp. 763–766, 2006, doi: 10.1109/TMAG.2006.872034.

[48] A. Lotfi and E. Rahimpour, “Optimum design of core blocks and analyzing the fringing effect in shunt reactors with distributed gapped-core,” *Electric Power Systems Research*, vol. 101, pp. 63–70, 2013, doi: 10.1016/j.epsr.2013.03.006.

[49] A. B. Nedić, M. v. Simović, Z. M. Lazarević, and S. D. Milić, “Implementation of minimisation techniques to construction optimisation of iron-core inductor,” *IET Electr Power Appl*, vol. 10, no. 1, pp. 9–17, Jan. 2016, doi: 10.1049/iet-epa.2014.0446.

[50] R. Sundaria *et al.*, “Effects of stator core welding on an induction machine – Measurements and modeling,” *J Magn Magn Mater*, vol. 499, Apr. 2020, doi: 10.1016/j.jmmm.2019.166280.

[51] R. Jez, “Influence of the Distributed Air Gap on the Parameters of an Industrial Inductor,” *IEEE Trans Magn*, vol. 53, no. 11, Nov. 2017, doi: 10.1109/TMAG.2017.2699120.

[52] A. Pulnikov, “Modification of Magnetic Properties of Non Oriented Electrical Steels by the Production of Electromagnetic Devices,” Doctoral thesis, Ghent University, Ghent, 2004.

[53] A. Schoppa, J. Schneider, C.-D. Wuppermann, and T. Bakon, “Influence of welding and sticking of laminations on the magnetic properties of non-oriented electrical steels,” *J Magn Magn Mater*, pp. 367–369, 2003.

[54] M. Bali and A. Muetze, “The degradation depth of electrical steel sheets due to mechanical and laser cutting,” in *2017 IEEE 11th International Symposium on Diagnostics for Electrical Machines, Power Electronics and Drives (SDEMPED)*, 2017, pp. 544–549. doi: 10.1109/DEMPED.2017.8062408.

[55] M. Hofmann, H. Naumoski, U. Herr, and H. G. Herzog, “Magnetic Properties of Electrical Steel Sheets in Respect of Cutting: Micromagnetic Analysis and Macromagnetic Modeling,” *IEEE Trans Magn*, vol. 52, no. 2, Feb. 2016, doi: 10.1109/TMAG.2015.2484280.

[56] A. Saleem, N. Alatawneh, T. Rahman, D. A. Lowther, and R. R. Chromik, “Effects of Laser Cutting on Microstructure and Magnetic Properties of Non-Orientation Electrical Steel Laminations,” *IEEE Trans Magn*, vol. 56, no. 12, Dec. 2020, doi: 10.1109/TMAG.2020.3029256.

APPENDIX A

```
%filter inductor design
clear all
clc

Lref = 10.6e-3;            % desired inductance
Iref = 5;                  % current
Ku = 0.4;                  % window utilisation factor
Jrms = 1.416e6;            % current density (2.12mm diameter winding wire)
Bamp = 1.0;                % desired flux density
mu0 = 4*pi*1e-7;           % permeability of free space
murlin = 7650;             % permeability of M330 35A electrical steel
ngap=2;                    % number of air gaps

% Material parameters
par_Cogent_M33035A;

% Conductor area
ACu = Iref/Jrms;           %copper cross sectional area
dCu = 2*sqrt(ACu/pi);      %copper diameter

% Analytical inductor design according to Kazimierczuk

ap = Lref*2*(Iref)^2/(Ku*sqrt(2)*Jrms*Bamp); % calculates area-product

nkd = 25;                                  % number of different possible kd
                                           % for each core height.
                                           % i.e. for each core height 25 possible ratios
                                           % between inner and outer diameter are
calculated

kd = linspace(1.4,2.6,nkd);                % ratio between inner & outer diameter of
core.

h = [12 13 15 20 25 30 35 40 50 60 70 80]*1e-3;   % core heights
[kd,h] = ndgrid(kd, h);

% Calculate inner diameter

di = (ap*8./(pi*h.*(kd-1))).^(1/3);


% Other parameters
do = kd.*di;               % core outer diamter
rin= di/2;                 % core inner radius
rout = do/2;               % core outer radius
w = (do-di)/2;             % core width
lFe = (do+di)/2*pi;        % Length of flux path
AFe = h.*w;                % Iron cross-section area
Aww = pi*di.^2/4;          % winding window area
N1 = round(Ku*Aww./ACu);   % Number of turns
```

```
% return
load -mat sF.matx          % COMSOL data

% iterate for air gap length

delta = mu0*AFe.*N1.^2/Lref - lFe/murlin;  % length of air gap on each side

% fringing factor iterations

for it = 1 : 100

  % Get L
  ind = (delta <= 0); delta_tmp = delta;
  Ff = reshape(interpn(sF.xx,sF.yy,sF.zz,sF.Ff, delta_tmp(:), kd(:), h(:), 'linear',
1),   size(kd));

  L = mu0*N1.^2.*AFe ./ (lFe/murlin + ngap*delta./Ff);

  % L with small change in delta
  dFf = reshape(interpn(sF.xx,sF.yy,sF.zz,sF.Ff, delta_tmp(:)+1e-6, kd(:), h(:),
'linear', 1), size(kd));
  dL = mu0*N1.^2.*AFe ./ (lFe/murlin + ngap*(delta+1e-6)./dFf);

  % residual and jacobian dL/d_delta
  jac = (dL-L)./1e-6;
  res = L-Lref;

  % incrementation
  ddelta = -res./jac;
  delta = delta + ddelta;

  % convergence check
  if all(abs(ddelta)./delta < 1e-6)
    break
  end

end
close

% build inductor set
% saves all designs in structure for use in simulation model
apset2 = toroidalInductor('ri', di/2, 'ro', do/2, 'h', h, 'N1', N1, 'delta', delta,
'dCu', dCu, 'mur', murlin, 'ngap', ngap, 'densFe', densFe, 'T', 20, 'Fftype', sF);
```

Published with MATLAB® R2022a

APPENDIX B

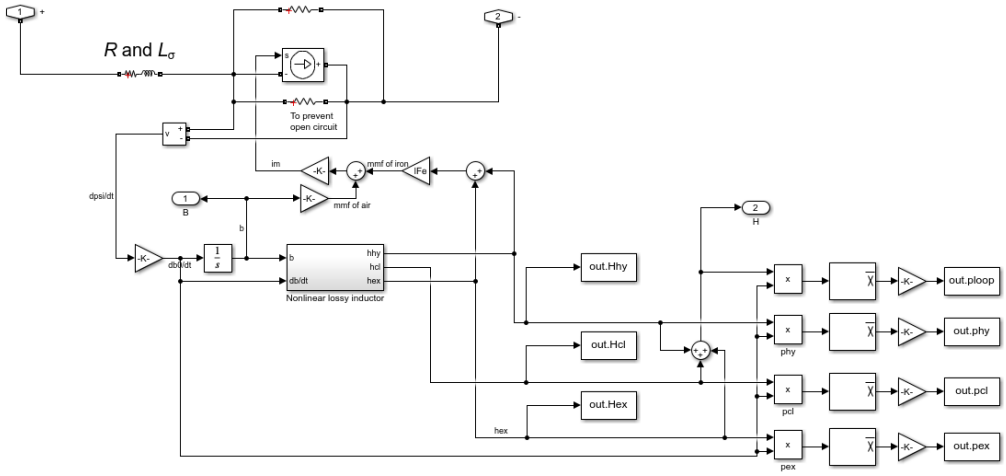

Figure 45: *Simulink inductor model*

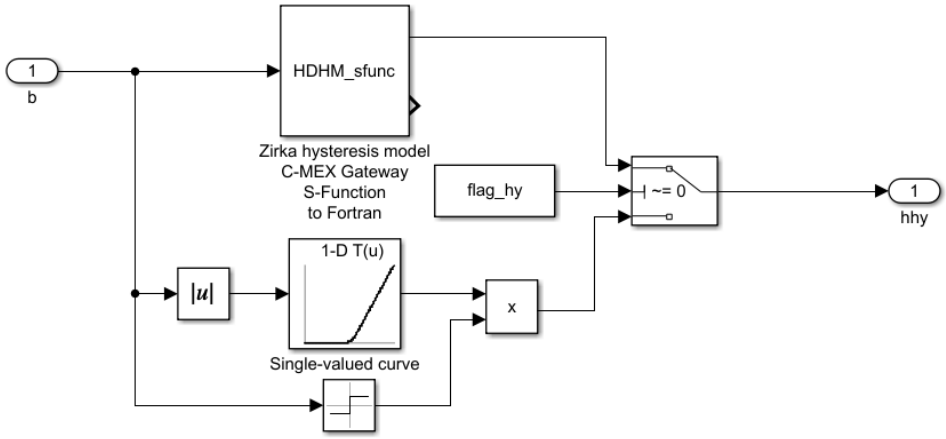

Figure 46: *Simulink hysteresis model*

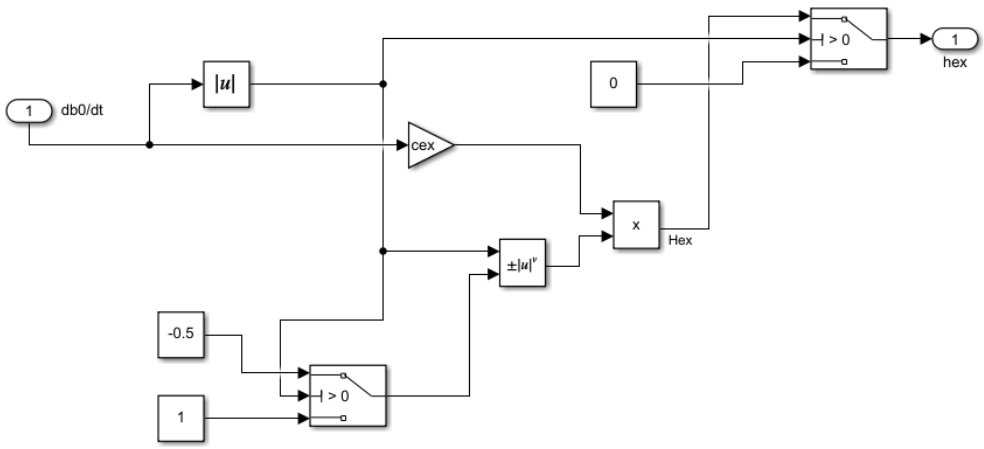

Figure 47: *Simulink excess losses model*